PROCEEDINGS A

royalsocietypublishing.org/journal/rspa

Research

Cite this article: Senhora FV, Menezes IFM, Paulino GH. 2023 Topology optimization with local stress constraints and continuously varying load direction and magnitude: towards practical applications. *Proc. R. Soc. A* **479**: 20220436.
https://doi.org/10.1098/rspa.2022.0436

Received: 22 June 2022
Accepted: 23 January 2023

Subject Areas:
civil engineering, mechanical engineering, structural engineering

Keywords:
topology optimization, stress constraints, multiple load case, worst-case, continuously varying load

Author for correspondence:
Glaucio H. Paulino
e-mail: gpaulino@princeton.edu

Electronic supplementary material is available online at https://doi.org/10.6084/m9.figshare.c.6423599.

THE ROYAL SOCIETY PUBLISHING

Topology optimization with local stress constraints and continuously varying load direction and magnitude: towards practical applications

Fernando V. Senhora[1,2], Ivan F. M. Menezes[1] and Glaucio H. Paulino[3,4]

[1]Pontifical Catholic University of Rio de Janeiro, Rua Marquês de São Vicente, 225, Rio de Janeiro 22453, Brazil
[2]School of Civil and Environmental Engineering, Georgia Institute of Technology, 790 Atlantic Drive, Atlanta, GA 30332, USA
[3]Department of Civil and Environmental Engineering, and
[4]Princeton Materials Institute (PMI), Princeton University, Princeton, NJ 08544, USA

GHP, 0000-0002-3493-6857

Topology optimization problems typically consider a single load case or a small, discrete number of load cases; however, practical structures are often subjected to infinitely many load cases that may vary in intensity, location and/or direction (e.g. moving/rotating loads or uncertain fixed loads). The variability of these loads significantly influences the stress distribution in a structure and should be considered during the design. We propose a locally stress-constrained topology optimization formulation that considers loads with continuously varying direction to ensure structural integrity under more realistic loading conditions. The problem is solved using an Augmented Lagrangian method, and the continuous range of load directions is incorporated through a series of analytic expressions that enables the computation of the worst-case maximum stress over all possible load directions. Variable load intensity is also handled by controlling the magnitude of load basis vectors used to derive the worst-case load. Several two- and three-dimensional examples demonstrate that topology-optimized designs are

extremely sensitive to loads that vary in direction. The designs generated by this formulation are safer, more reliable, and more suitable for real applications, because they consider realistic loading conditions.

1. Introduction

Engineering structures are subjected to a multitude of loads over their lifespan [1]. For example, aircraft are subjected to constantly varying inertial loads; buildings are subjected to continuously varying wind and live loads, in addition to the structure's self-weight. These myriads of loading conditions cause an equally countless number of stress distributions that should be considered in the design process to guarantee structural integrity. Nevertheless, topology optimization typically focuses on structures with a single load case or a small number of load cases, leading to designs that are over-fitted to an artificial single loading condition, and that are not robust under the service loads.

In this work, we focus on loads that vary in direction and magnitude, while retaining a fixed location of application. Figure 1 exemplifies all the load varying cases contemplated in this work, i.e. loads varying in direction and magnitude (figure 1*a*), loads varying only in direction (figure 1*b*), loads varying in a limited range of directions (figure 1*c*), loads varying in direction combined with fixed loads (figure 1*d*), two or more loads varying independently (figure 1*e*) and loads varying in three dimensions (figure 1*f*). We formulate the stress constrained topology optimization problem such that the local stress constraints account for the load variability in a worst-case-oriented approach. That is, the stress constraints consider the maximum stress generated by the loads in a set of possible load directions. We derive analytic expressions that represent the maximum stress in this set of load directions. The formulation is tailored for linear elasticity (state equation) and we adopt a von Mises stress measure.

To handle the large number of constraints inherent to the local stress constraints problem, we use the AL-based approach adapted from [2]. We highlight that although this work focuses on stress constraints, the analytic expressions derived here can be applied to any topology optimization problem with bilinear functions and linear state equations (see SS5 of the electronic supplementary material for derivations related to compliance minimization).

The remainder of this paper is organized as follows. Section 2 reviews the existing literature on stress-constrained topology optimization considering multiple load cases. Section 3 briefly presents the local stress constrained topology optimization formulation used in this work. Section 4 presents a boundary corrected version of the filter proposed in this work. Section 5 describes the multiple load direction framework with detailed derivations of the proposed analytic solutions for worst-case stress. Section 6 presents a generalization of load decomposition and varying load intensity. Section 7 summarizes the formulation by presenting the general topology optimization formulation, and the respective AL method sub-problem used in this work. Section 8 provides benchmark numerical examples obtained with the proposed method, and §9 presents concluding remarks. Table 1 presents the nomenclature used in this manuscript. Additionally, we provide, in the electronic supplementary material, the details of the implementation (§S1), the optimization algorithm (§S2), the convergence plots of the numerical results (§S3), derivation of the sensitivity of the proposed formulation (§S4) and the derivations to consider multiple load directions in the compliance minimization problem (electronic supplementary material, §S5).

2. Related work

The simplest way to incorporate multiple load cases in a stress-constrained TO formulation is to consider additional constraints for each load case; however, each additional load

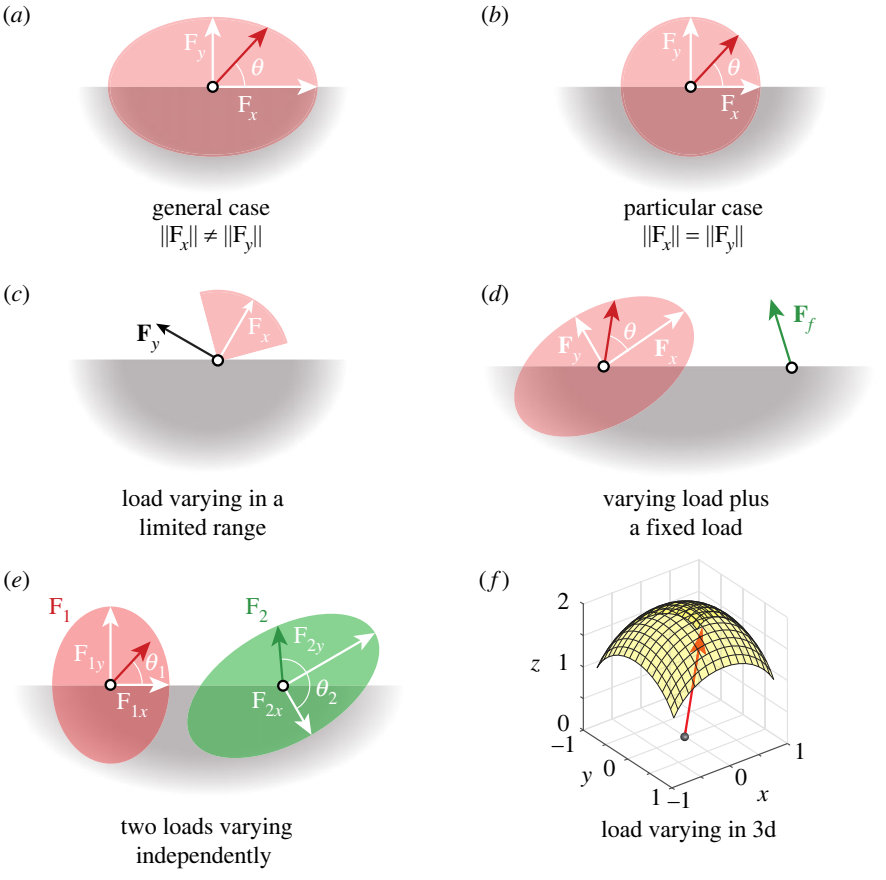

Figure 1. Schematic of all the load conditions, with loads varying in direction and magnitude, contemplated in the proposed formulation. (*a*) Load varying 360° forming a ellipsoid domain in which the load varies, not only in direction, but also in magnitude. (*b*) Load varying 360° forming a circular domain, in which the load varies only in direction. (*c*) Load varying in a limited range of admissible directions. (*d*) Load varying 360° combined with a fixed load. (*e*) Two loads varying independently in direction. (*f*) Load varying in three-dimensional directions.

Table 1. Nomenclature.

$\widetilde{\sigma}_j^v$	maximum of the von Mises stress at the centroid of element *j* considering all possible load angles
β	parameter that controls the sharpness of the Heaviside projection function (the higher the value the sharper the projection)
$\boldsymbol{\lambda}^{(k)}$	vector of approximated Lagrange multipliers at the *k*th iteration of the AL method
$\boldsymbol{\rho}$	vector of filtered densities
$\boldsymbol{\sigma}_x$ and $\boldsymbol{\sigma}_y$	stress components
$\boldsymbol{\theta}_j^{\sigma}$	critical angle of the loads that causes the highest stress in the structure
$\boldsymbol{\xi}$	adjoint vector used for sensitivity evaluation
ϵ	ersatz stiffness
η	scale factor used in the modified AL function (3.6)
Γ	domain of admissible load angles
$[-\theta_r, \theta_r]$	range of admissible angles

(*Continued*.)

Table 1. (*Continued*.)

$\mu^{(k)}$	penalty parameter at the *k*th iteration of the AL method
ν	Poisson's ratio of solid material
$\sigma_j^v(\mathsf{z}, \boldsymbol{\theta})$	von Mises stress at the centroid of element *j*
σ_{lim}	stress limit for a given material
τ_{ij}	part of the expression for the von Mises stress associated with loads *i* and *j*
θ	load angle
$\theta_{low}, \theta_{up}$	lower and upper limit of the range of admissible angles
$\tilde{\rho}_e$	volume fraction of element *e*
$\widehat{\sigma}^v$	upper bound for the critical stress $\widetilde{\sigma}^v$
$\mathop{\mathbb{A}}_{e=1}^{N_e}$	assembly information of the global stiffness matrix
C	compliance
E_0	Young's modulus of solid material
$\mathbf{F}(\boldsymbol{\theta})$	load vector
FEA	finite-element analysis
$\mathbf{F}_f$	load basis vectors associated with a fixed load
$\mathbf{F}_x$ and $\mathbf{F}_y$	load basis vectors
$g_j(\mathbf{z})$	*j*th stress constraint
g_V	volume constraint
$J^{(k)}(\mathbf{z})$	augmented Lagrangian function at iteration *k*
$\mathsf{K}(\mathbf{z})$	stiffness matrix
k_0	the local stiffness matrix of a solid element
k_e	the *e*th element local stiffness matrix
$M(\mathbf{z})$	mass (volume) of the structure
N_c	number of stress constraints
N_e	number of elements
$\mathbf{P}$	filter matrix
p	penalization parameter of the SIMP formulation
R	the radius of the filter that controls the minimum length scale
t_{ij}	quadratic stress terms of the load basis vectors *i* and *j*
SIMP	solid isotropic material with penalization
s_{ij}	quadratic stress terms associated with the crossed load basis terms
TO	topology optimization
U	displacement vector
V	von Mises matrix
v_e	area (for two-dimensional problems) or volume (for three-dimensional problems) of element *e*
$\mathsf{x}_i^\star, \mathsf{x}_j^\star$	position of the centroid of the *i*th and *j*th elements, respectively
z	vector of design variables

case substantially increases the computational cost, rendering it impossible to account for continuously varying loads. Thus, this approach has typically been limited to no more than two fixed load cases [2–6]. Alternatively, the problem with multiple load cases has been formulated as an uncertainty in the load, which can be solved using stochastic or worst-case-oriented deterministic approaches [7,8].

In the stochastic approach, the load is treated as a random variable following a known probability distribution, and the objective and/or constraints of the optimization problem are modelled as statistical moments of random functions or as probabilities. Stochastic models have been widely applied to compliance-based TO problems [9–17], but more moderately so for stress-based TO [18–21]. Kanno & Takewaki [19] studied the effects of multiple load directions with stress constraints in the context of ground structure topology optimization using a probabilistic model to generate a sample load that represents the possible load cases. Lógó *et al.* [20] worked on the optimal conditions of multiple load cases and proposed a probabilistic model to address the problem with trusses. Luo *et al.* [21] considered uncertainty in the material and in the load amplitude by using reliability based topology optimization. Stochastic approaches, however, are troublesome in practice because they demand large data samples to obtain accurate results, which leads to high computational costs. The high computational cost can be mitigated using surrogate models [22], but this increases the complexity of the implementation. In addition, stochastic techniques can cause instability in the optimization procedure [23].

On the other hand, worst-case-oriented approaches are equivalent to solving an optimization in the set of possible load cases in which the worst case is identified, and used as the objective and/or constraint function in the TO problem. The solution to the worst-case-oriented problem guarantees an upper bound for the objective function (in the case of minimization problems), and/or the satisfaction of the constraints for any load case considered in the set of possible load cases. Thore *et al.* [8] provide a worst-case-oriented general framework for quadratic objective functions and quadratic constraints under load uncertainty by recasting the problem as a nonlinear, semi-definite programming problem which is then solved numerically. Young *et al.* [24] and Xie & Steven [25] use an evolutionary structural optimization approach and consider multiple load cases with stress constraints by performing a finite-element analysis for each load case. Csébfalvi [26] deals specifically with uncertainty in load directions with an iterative approach. Holmberg *et al.* [27] proposed a game theory approach to solve the worst-case-oriented stress constraints problems considering variation in the load direction; however, because the problems are non-convex, the existence of Nash equilibrium to the game problem proposed by Holmberg *et al.* [27] is not guaranteed, and they rely on empirical observation of the numerical results. In the subsequent work, Thore *et al.* [28] modelled the problem as a Stackelberg game, instead of a zero-sum game, and showed that, with this interpretation, it is possible to guarantee the existence of a solution to the problem. However, the numerical methodology to solve the Stackelberg game problem can be computationally inefficient.

In this work, we propose a worst-case-oriented approach, but, unlike the previously mentioned approaches, we use the linear state equations and the bilinear properties of the von Mises stress to derive an *analytic* solution for the worst-case stress caused by continuously varying loads. We then use these worst-case stresses as the local stress constraints in the TO problem. These *analytic* solutions, which are one of the main contributions of this work, are accurate, computationally efficient, and guarantee the structural integrity of the final design over the set of continuously varying loading conditions.

3. Theoretical formulation

The proposed formulation for stress-constrained topology optimization with continuously varying load directions is stated as follows:

$$\left.\begin{aligned} \min_{\mathbf{z}} M(\mathbf{z}) &= \sum_{e=1}^{N_e} \tilde{\rho}_e v_e \\ \text{s.t.: } g_j(\mathbf{z}, \boldsymbol{\theta}) &\le 0, \quad j = 1, \ldots, N_c \\ 0 \le z_e &\le 1, \quad e = 1, \ldots, N_e \\ \text{with: } \mathbf{K}(\mathbf{z})\mathbf{U} &= \mathbf{F}(\boldsymbol{\theta}) \\ \tilde{\boldsymbol{\rho}}(\mathbf{z}) &= \mathcal{H}(\mathbf{P}\mathbf{z}) \end{aligned}\right\} \tag{3.1}$$

where $M(\mathbf{z})$ is the mass (volume) of the structure, $\mathbf{z}$ is the vector of design variables, which represents the material density at each point in the domain, $\tilde{\rho}_e$ is the volume fraction of element e defined using a smooth Heaviside projection [29], $\boldsymbol{\rho}(\mathbf{z}) = \mathbf{P}\mathbf{z}$ is the vector of filtered densities, $\mathbf{P}$ is the filter matrix, v_e is the area (for two-dimensional problems) or volume (for three-dimensional problems) of element e, $g_j(\mathbf{z}, \boldsymbol{\theta})$ is the jth stress constraint, which depends not only on the design variables $\mathbf{z}$, but also on the load direction determined by θ, N_c is the number of stress constraints, N_e is the number of elements in the finite-element mesh, and $\mathbf{K}(\mathbf{z})\mathbf{U} = \mathbf{F}(\boldsymbol{\theta})$ is the linear elastic state equation, where the right-hand side varies with the angle of the load, $\boldsymbol{\theta}$, which is defined by the problem. The explanation of variable θ and its range is displayed in figure 1. Note that the optimization problem presented in equation (3.1) admits a trivial solution $\mathbf{z} = \mathbf{0}$. Numerically, however, this solution is almost never achieved given a reasonable initial guess for the problem (i.e. an initial guess in which $\mathbf{z} \neq \mathbf{0}$).

The physical density vector, denoted by $\tilde{\boldsymbol{\rho}}$, is obtained by first applying a boundary corrected *polynomial filter*, described in §4, and then the Heaviside operation [30] to the design variable $\mathbf{z}$. The filter operation is computed by multiplying the design variable vector $\mathbf{z}$ by the filter matrix $\mathbf{P}$:

$$\boldsymbol{\rho} = \mathbf{P}\mathbf{z} \tag{3.2}$$

where the filtered variables, $\boldsymbol{\rho}$, are defined for convenient notation. After we apply the filter operation, we perform the smooth Heaviside projection [30]:

$$\tilde{\boldsymbol{\rho}} = \mathcal{H}(\boldsymbol{\rho}) = \frac{\tanh(\beta\eta) + \tanh(\beta(\boldsymbol{\rho} - \eta))}{\tanh(\beta\eta) + \tanh(\beta(1 - \eta))} \tag{3.3}$$

where $\eta = 0.5$ is the value of the threshold for the Heaviside function and β controls the sharpness of such a function. We use an element-based density approach, in which the stiffness of an element is defined using the solid isotropic material with penalization (SIMP) method [31,32], and the stiffness matrix, $\mathbf{K}$, is defined as:

$$\mathbf{K}(\mathbf{z}) = \mathop{\mathbb{A}}_{e=1}^{N_e} \mathbf{k}_e, \quad \text{with } \mathbf{k}_e = E_e \mathbf{k}_0, \; E_e = \epsilon + (1 - \epsilon)\tilde{\rho}_e^p \tag{3.4}$$

where $\mathbf{k}_e$ are the element local stiffness matrices, ϵ represents an Ersatz stiffness that prevents the stiffness matrix from becoming singular, p is the SIMP penalization factor that penalizes intermediate densities, $\mathbf{k}_0$ is the stiffness matrix for a solid element, E_e is the material interpolation stiffness function, and the symbol $\mathop{\mathbb{A}}_{e=1}^{N_e}$ represents the assembly process of the global stiffness matrix. The stress constraint formulation used here is a slight variation of the one proposed by [2,33] and is defined as:

$$g_j(\mathbf{z}) = \begin{cases} \tilde{\rho}_j^p \left[\left(\dfrac{\sigma_j^v}{\sigma_{\text{lim}}} - 1 \right) + \left(\dfrac{\sigma_j^v}{\sigma_{\text{lim}}} - 1 \right)^2 \right] & \text{if } \dfrac{\sigma_j^v}{\sigma_{\text{lim}}} > 1 \\ \tilde{\rho}_j^p \left(\dfrac{\sigma_j^v}{\sigma_{\text{lim}}} - 1 \right) & \text{otherwise,} \end{cases} \tag{3.5}$$

where the exponent p is the SIMP penalization factor, σ_j^v is the von Mises stress at element j, and σ_{lim} is the stress limit. The optimization formulation used in this work adopts one stress

constraint for each element of the FEM mesh in which the stress is evaluated at the centroid of the element (i.e. $N_e = N_c$). We solve the optimization problem in equation (3.1) using a modified version of the Augmented Lagrangian (AL) method [34,35] described in [2]. In the AL method, we solve a sequence of k-subproblems for which the solution converges to an optimum of the original problem. In the modified AL method described in [2], the authors introduced two new parameters: γ_e, which is adaptively adjusted during the optimization procedure to overcome local optima; and η, which scales the penalty terms of the AL function according to the number of constraints. However, in this work, we have eliminated the use of variable γ_e. The modified AL function is defined as:

$$\left.\begin{aligned} J^{(k)}(\mathbf{z}) &= \sum_{e=1}^{N_e} \tilde{\rho}_e v_e + \eta \sum_{j=1}^{N_c} \left[\lambda_j^{(k)} h_j(\mathbf{z}) + \frac{\mu^{(k)}}{2} h_j(\mathbf{z})^2 \right] \\ \text{and} \qquad h_j(\mathbf{z}, \widehat{\sigma}^v(\boldsymbol{\theta}^\star)) &= \max \left[g_j(\mathbf{z}, \widehat{\sigma}^v(\boldsymbol{\theta}^\star)), -\frac{\lambda_j^{(k)}}{\mu^{(k)}} \right]. \end{aligned}\right\} \tag{3.6}$$

For a detailed explanation of the modified AL method, see [2].

4. Boundary corrected filter

Traditional filters [36,37] present a strong bias towards the boundaries of the TO domain [38–41], because the structural optimized features connected to the boundaries are only subjected to half of the minimum length-scale. To correct this boundary bias, padding strategies, which add an exterior layer of passive void elements around the domain, have been proposed [38–40]. However, these padding strategies can be troublesome for domains with complex geometries, especially for three-dimensional problems. We propose a corrected version of the *polynomial filter* to address the boundary bias. In this corrected version, we modify the denominator of the traditional *polynomial filter* [36,37], as displayed in equations (4.1) and (4.2):

$$P_{ij} = \frac{w_{ij} v_j}{\psi_i}, \quad \text{with } w_{ij} = \max \left[0, \left(1 - \frac{||\mathbf{x}_i - \mathbf{x}_j||_2}{r} \right) \right]^s, \tag{4.1}$$

and

$$\psi_i = \begin{cases} \sum_{k=1}^{N_e} w_{ik} v_k, & \text{If the element is less than } r \text{ distance from a boundary that has load or support prescribed to it} \\ \max \left\{ \sum_{k=1}^{N_e} w_{mk} v_k \mid m = 1, \ldots, N_e \right\}, & \text{Otherwise,} \end{cases} \tag{4.2}$$

where r is the filter radius, and $||\mathbf{x}_i - \mathbf{x}_j||_2$ represents the distance between the centroids, $\mathbf{x}_i$ and $\mathbf{x}_j$, of elements i and j, respectively. The order of the filter is defined by the filter exponent, s. The correction of the denominator term ψ_i means that the rows associated with elements, which are less than r distance from the edge, and more than r distance from a boundary condition, will sum up to less than one. This correction implicitly behaves like a padding of void elements without the need to explicitly add the exterior layer of padding elements [38–40].

5. Continuously varying load direction

In this work, the direction of the loads applied to the TO domain is controlled by a variable $\boldsymbol{\theta} \in \Gamma$, which represents the angle of the load application, and by the set Γ that represents the set of all possible angles. Each load direction, a.k.a. load angle $\boldsymbol{\theta} \in \Gamma$, induces a distinct stress state in

the optimized structure. To prevent structural failure, we have to consider the maximum stress induced by all possible load angles, $\boldsymbol{\theta} \in \Gamma$, i.e. the critical stress:

$$\tilde{\sigma}_j^v = \sup\left\{\sigma_j^v(\mathbf{z}, \boldsymbol{\theta}) \mid \boldsymbol{\theta} \in \Gamma\right\} \tag{5.1}$$

where $\sigma_j^v(\mathbf{z}, \boldsymbol{\theta})$ is the von Mises stress at the centroid of the element j of the FEM mesh, which depends on the design variables, $\mathbf{z}$, i.e. the structure, and the load direction, $\boldsymbol{\theta}$. We can cast the problem of finding the critical stress generated by $\boldsymbol{\theta}$ as an optimization problem:

$$\left.\begin{aligned} &\max_{\boldsymbol{\theta}\in\Gamma} \sigma_j^v(\mathbf{z}, \boldsymbol{\theta}) \\ &\text{with: } \mathbf{K}(\mathbf{z})\mathbf{U} = \mathbf{F}(\boldsymbol{\theta}). \end{aligned}\right\} \tag{5.2}$$

In other words, we are interested in the critical angles, $\boldsymbol{\theta}_j^{\mathrm{cr}}$, that cause the highest stress in the structure. Notice that each stress evaluation point j, and, therefore, each constraint will have a particular critical angle. Using the critical angles, θ_j^{cr}, $j = 1, \ldots, N_c$, we can analytically derive a worst-case stress constraint for each constraint, g_j, $j = 1, \ldots, Nc$, in the TO problem, which now reads:

$$\left.\begin{aligned} &\min_{\mathbf{z}} M(\mathbf{z}) = \sum_{e=1}^{N_e} \tilde{\rho}_e v_e \\ &\text{s.t.: } \max_{\boldsymbol{\theta}} g_j(\mathbf{z}, \boldsymbol{\theta}) \le 0, j = 1, \ldots, N_c \\ &\quad 0 \le z_e \le 1, \quad e = 1, \ldots, N_e \\ &\text{with: } \mathbf{K}(\mathbf{z})\mathbf{U} = \mathbf{F}(\boldsymbol{\theta}) \\ &\quad \tilde{\boldsymbol{\rho}}(\mathbf{z}) = \mathcal{H}(\mathbf{P}\mathbf{z}). \end{aligned}\right\} \tag{5.3}$$

In the next sections, we derive solutions for the problem in equation (5.2) considering different sets of admissible load angles, that is, different domains, Γ.

(a) Case 1: planar load varying in an arbitrary range

We begin by deriving the solution for the problem in equation (5.2) considering a single load varying in direction within a limited range of angles, $\theta \in [\theta_{\mathrm{low}}, \theta_{\mathrm{up}}]$, contained inside $[-\pi, \pi]$.[1] We start by writing the load as the sum of two vectors weighted by cosine and sine functions:

$$\mathbf{F}(\theta) = \mathbf{F}_x \cos(\theta) + \mathbf{F}_y \sin(\theta) \tag{5.4}$$

where the load basis vectors, $\mathbf{F}_x$ and $\mathbf{F}_y$, are two linearly independent vectors that compose the space of admissible loads. We highlight that $\mathbf{F}_x$ and $\mathbf{F}_y$ do not need to be aligned with the x-axis or the y-axis, or have the same magnitude. The load basis vectors just need to be able to span the space of possible load cases, as the following derivations do **not** rely on orthogonality, or any special property of the $\mathbf{F}_x$ and $\mathbf{F}_y$ vector. However, the θ parameter only has a physical counterpart (i.e. the angle of the resulting load) when $\mathbf{F}_x$ and $\mathbf{F}_y$ are defined as a right-handed orthogonal positive coordinate system. Figure 2 displays a schematic of the domain of possible loads, and the load basis vectors.

Owing to the linearity of the underlying physics (linear elasticity), we can compute the solution to the state equations using the load basis vectors as:

$$\mathbf{U} = \mathbf{K}^{-1}\mathbf{F}(\theta) = (\mathbf{K}^{-1}\mathbf{F}_x)\cos(\theta) + (\mathbf{K}^{-1}\mathbf{F}_y)\sin(\theta). \tag{5.5}$$

By defining $\mathbf{U}_x = \mathbf{K}^{-1}\mathbf{F}_x$ and $\mathbf{U}_y = \mathbf{K}^{-1}\mathbf{F}_y$, we can compute the stress as:

$$\boldsymbol{\sigma} = \mathbf{D}\mathbf{B}\mathbf{U} = \mathbf{D}\mathbf{B}(\mathbf{U}_x \cos(\theta) + \mathbf{U}_y \sin(\theta)) \quad \text{and} \quad \boldsymbol{\sigma} = \boldsymbol{\sigma}_x \cos(\theta) + \boldsymbol{\sigma}_y \sin(\theta), \tag{5.6}$$

[1]We choose the domain as $[-\pi, \pi]$ instead of the more obvious $[0, 2\pi]$ because of the definition of the inverse tangent used in this paper, which has an image in the range $[-\pi, \pi]$.

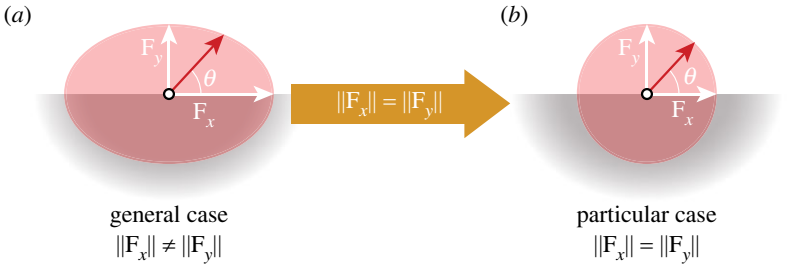

Figure 2. Schematic of the domain of possible load cases in red and the load vector basis in white for case 1, with (*a*) general load basis vector, i.e. $||F_x|| \neq ||F_y||$ forming a ellipsoid domain in which the load varies, not only in direction, but also in magnitude, and (*b*) load basis vectors with the same magnitude, i.e. $||F_x|| = ||F_y||$ forming a circular domain, in which the load varies only in direction.

where **D** and **B** are the constitutive and strain-displacement matrices, respectively, in the finite-element setting. We defined the stress components as $\boldsymbol{\sigma}_x = \mathbf{DBU}_x$ and $\boldsymbol{\sigma}_y = \mathbf{DBU}_y$, which allow us to compute the von Mises stress as:

$$\left.\begin{aligned} \sigma^v &= \{\sigma^T \mathbf{V} \sigma\}^{1/2} \\ &= \{[\boldsymbol{\sigma}_x \cos(\theta) + \boldsymbol{\sigma}_y \sin(\theta)]^T \, \mathbf{V} [\boldsymbol{\sigma}_x \cos(\theta) + \boldsymbol{\sigma}_y \sin(\theta)]\}^{1/2} \\ \text{and} \quad \sigma^v &= \{t_{xx} \cos^2(\theta) + t_{yy} \sin^2(\theta) + 2t_{xy} \cos(\theta) \sin(\theta)\}^{1/2} \end{aligned}\right\} \tag{5.7}$$

where **V** is the von Mises matrix, and we defined the quadratic stress terms $t_{xx} = \boldsymbol{\sigma}_x^T \mathbf{V} \boldsymbol{\sigma}_x$, $t_{yy} = \boldsymbol{\sigma}_y^T \mathbf{V} \boldsymbol{\sigma}_y$ and $t_{xy} = \boldsymbol{\sigma}_x^T \mathbf{V} \boldsymbol{\sigma}_y$ to simplify the expression. Notice that t_{xx}, t_{yy} and t_{xy} do not depend on θ. We simplify equation (5.7) using trigonometric identities:

$$\sigma^v = \{t_{xy} \sin(2\theta) + 0.5[(t_{xx} - t_{yy}) \cos(2\theta) + t_{xx} + t_{yy}]\}^{1/2} \tag{5.8}$$

We change the definition of the objective function in equation (5.2) to the squared von Mises stress. Squaring the von Mises stress simplifies further computations, and, because the von Mises stress is non-negative, squaring it will not change the solution to the maximization problem. Therefore, the optimization problem for the critical load angle can then be written as:

$$\left.\begin{aligned} &\max_{\theta \in [\theta_{\text{low}}, \theta_{\text{up}}]} [\sigma^v(\mathbf{z}, \theta)]^2 \\ &\text{with: } \mathbf{K}(\mathbf{z})\mathbf{U}_x = \mathbf{F}_x, \quad \mathbf{K}(\mathbf{z})\mathbf{U}_y = \mathbf{F}_y. \end{aligned}\right\} \tag{5.9}$$

To find the analytic solution to the optimization problem in equation (5.9) we differentiate the objective function with respect to θ, and set it equal to zero to find the critical points:

$$\frac{\partial (\sigma^v)^2}{\partial \theta} = 2t_{xy} \cos(2\theta) - (t_{xx} - t_{yy}) \sin(2\theta) = 0. \tag{5.10}$$

Equation (5.10) solutions are of the form:

$$\theta^{\text{cr}} = \begin{cases} \frac{1}{2} \tan^{-1}(2t_{xy}, t_{xx} - t_{yy}) + k\pi & \text{for } k \in \mathbb{Z} \\ \frac{1}{2} \tan^{-1}(-2t_{xy}, t_{yy} - t_{xx}) + k\pi & \text{for } k \in \mathbb{Z}, \end{cases} \tag{5.11}$$

where $\tan^{-1}(\cdot, \cdot)$ is the two-value-argument inverse tangent that considers the appropriate quadrant in the computation of the inverse of the tangent. We denote the first and second set of solutions, in equation (5.11), as $\theta^{\text{cr}}_{\text{max}}$ and $\theta^{\text{cr}}_{\text{min}}$, respectively. Notice that all elements of the set $\theta^{\text{cr}}_{\text{max}}$ achieve the same value for the objective function, independently of the value of k, and the same is true for $\theta^{\text{cr}}_{\text{min}}$. Therefore, from now on, we will assume $k = 0$, meaning that the solution

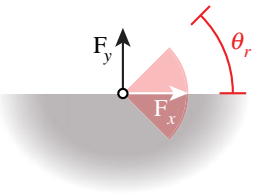

Figure 3. Schematic of the domain of possible load cases in red and the load vector basis in white (F_x) and black (F_y), with a limited range of angles (θ_r), for case 2.

will always lie in the interval $[-\pi, \pi]$. To classify these two critical points, θ^{cr}_{max} and θ^{cr}_{min}, we will use the second derivative:

$$\frac{\partial^2(\sigma^v)^2}{\partial\theta^2} = -4t_{xy}\sin(2\theta) - 2(t_{xx} - t_{yy})\cos(2\theta). \tag{5.12}$$

We can use the trigonometric identities:

$$\sin(\tan^{-1}(a,b)) = \frac{a}{\{a^2+b^2\}^{1/2}} \quad \text{and} \quad \cos(\tan^{-1}(a,b)) = \frac{b}{\{a^2+b^2\}^{1/2}}, \tag{5.13}$$

to obtain the value of the second derivative at θ^{cr}_{max} and θ^{cr}_{min}:

$$\left.\frac{\partial^2(\sigma^v)^2}{\partial\theta^2}\right|_{\theta=\theta^{cr}_{max}} = \frac{-8t_{xy}^2 - 2(t_{xx}-t_{yy})^2}{\left\{4t_{xy}^2 + (t_{xx}-t_{yy})^2\right\}^{1/2}} \tag{5.14}$$

and

$$\left.\frac{\partial^2(\sigma^v)^2}{\partial\theta^2}\right|_{\theta=\theta^{cr}_{min}} = \frac{8t_{xy}^2 + 2(t_{xx}-t_{yy})^2}{\left\{4t_{xy}^2 + (t_{xx}-t_{yy})^2\right\}^{1/2}}. \tag{5.15}$$

Notice that the second derivative in θ^{cr}_{max} is always non-positive, while the second derivative in θ^{cr}_{min} is always non-negative, meaning that θ^{cr}_{max} is a local maximum and θ^{cr}_{min} is a local minimum. Furthermore, the objective function is periodic, with the period equal to π, and the objective function is smooth, which means that the global maximum and global minimum are necessarily critical points. Since θ^{cr}_{max} and θ^{cr}_{min} are the only two critical points of the objective function, we have that θ^{cr}_{max} is a global maximum, and θ^{cr}_{min} is a global minimum. However, this solution does not take into account the limited range of angle that we consider in our optimization problem in equation (5.9). To consider the angle range in the solution, first, we will address the special instance where the angle range is centred at $\theta = 0$ described as $[-\theta_r, \theta_r]$, and displayed in figure 3. Then we will show how to generalize this special instance of angle range to any interval of the form $[\theta_{low}, \theta_{up}]$.

We can divide the solution of this problem into three instances. The first instance is when the critical point θ^{cr}_{max} lies in the interval $[-\theta_r, \theta_r]$, the second instance is when $[-\theta_r, \theta_r]$ lies between θ^{cr}_{min} and θ^{cr}_{max}, and the third instance is when θ^{cr}_{min} lies in the interval $[-\pi/2, \pi/2]$ and θ^{cr}_{max} does not. For the first instance, if the critical point θ^{cr}_{max} lies in $[-\theta_r, \theta_r]$, then θ^{cr}_{max}, as defined in equation (5.16), is the optimum point of this problem. However, if $\theta^{cr}_{max} \notin [-\theta_r, \theta_r]$, the optimum point is either $-\theta_r$ or θ_r, because we proved that the only other form of critical point of this problem is a global minimum. To determine which of $-\theta_r$ or θ_r is the optimum of the problem, first notice that the objective function is periodic, with a period of π. Therefore, we only have to focus in intervals smaller than $[-\pi/2, \pi/2]$; any larger interval will necessarily contain θ^{cr}_{max} because of the periodicity of the objective function. In the second instance, i.e. $[-\theta_r, \theta_r]$ lies between θ^{cr}_{min} and θ^{cr}_{max}, we can use the fact that the objective function is monotonic in the interval between θ^{cr}_{min} and θ^{cr}_{max} to conclude that the maximum is the point, $-\theta_r$ or θ_r, that is closest to θ^{cr}_{max}. In the

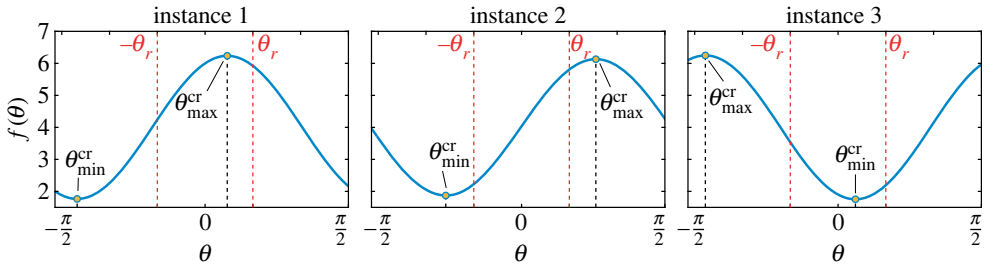

Figure 4. Representation of the three instances of the limited angle optimization problem. Instance 1, in which the maximum lies between the limited angle range ($[-\theta_r, \theta_r]$). Instance 2, in which the maximum and the minimum lie outside the limited angle range. Instance 3, in which the maximum lies outside and the minimum lies inside the limited angle range.

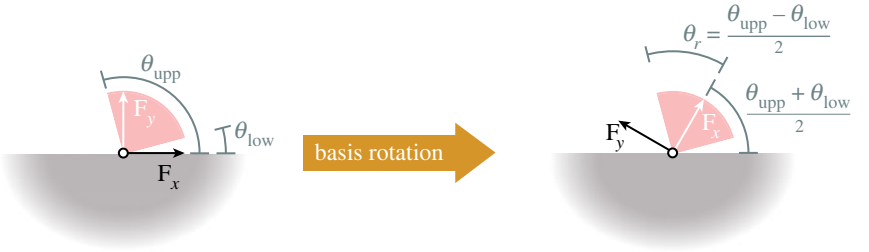

Figure 5. Schematic displaying how to rotate the basis vectors (F_x and F_y) to achieve any continuous range of admissible angles desired.

third instance θ^{cr}_{min} is in the interval $[-\theta_r, \theta_r]$, we can use the fact that the objective function is symmetric with respect to θ^{cr}_{min} to conclude that the farthest point from θ^{cr}_{min} inside $[-\theta_r, \theta_r]$ is the maximum, which, consequently, is also the point that is closest to θ^{cr}_{max}. For a clear visualization of the proof outlined above see figure 4. We can express all of these cases in a simple expression for the solution to the optimization problem in equation (5.9) as:

$$\theta^\star = \min\left\{\max\left[\frac{1}{2}\tan^{-1}(2t_{xy}, t_{xx} - t_{yy}), -\theta_r\right], \theta_r\right\}. \tag{5.16}$$

To generalize this solution for any value of $[\theta_{low}, \theta_{up}]$, we take advantage of the freedom that we have to choose the basis vectors $\mathbf{F}_x$ and $\mathbf{F}_y$ (for more details, see §6). We use this freedom to rotate $\mathbf{F}_x$ and $\mathbf{F}_y$, by the angle $(\theta_{up} + \theta_{low})/2$, so that $\mathbf{F}_x$ lies in the middle of the interval $[\theta_{low}, \theta_{up}]$, and we set $\theta_r = (\theta_{up} - \theta_{low})/2$, so that the interval $[-\theta_r, \theta_r]$ matches the original interval $[\theta_{low}, \theta_{up}]$, as illustrated in figure 5. With this change of basis, the problem of finding $\widetilde{\sigma}^v$ in the interval $[\theta_{low}, \theta_{up}]$ is the same as finding $\widetilde{\sigma}^v$ in the interval $[-\theta_r, \theta_r]$ with the rotated $\mathbf{F}_x$ and $\mathbf{F}_y$.

We substitute the expression of $\theta^\star$ into equation (5.8) of the von Mises stress to obtain the expression for the critical stress. This critical stress $\widetilde{\sigma}^v$ is used in the stress constraints in equation (3.5) to solve the topology optimization problem. This critical stress constraint guarantees that the von Mises stress will be below the stress limit for any load angle in the domain Γ in the optimized structure.

(i) Secondary range of admissible angles

If we obtain a solution that satisfies the stress constraints for a range of $[-\theta_r, \theta_r]$, then the solution will also satisfy the stress criteria for $\theta' = \theta + \pi$, in which $\theta \in [-\theta_r, \theta_r]$. This secondary range of admissible load angles occurs because the state equations are linear and the von Mises stress equation is the square root of a bilinear function. This idea comes naturally if one realizes that

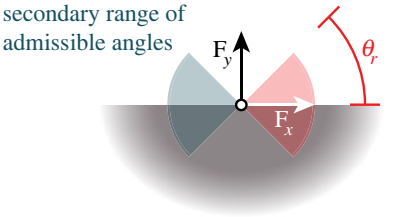

Figure 6. Schematic of the secondary range of admissible angles caused by the linearity of the state equations and the quadratic behaviour of the von Mises stress.

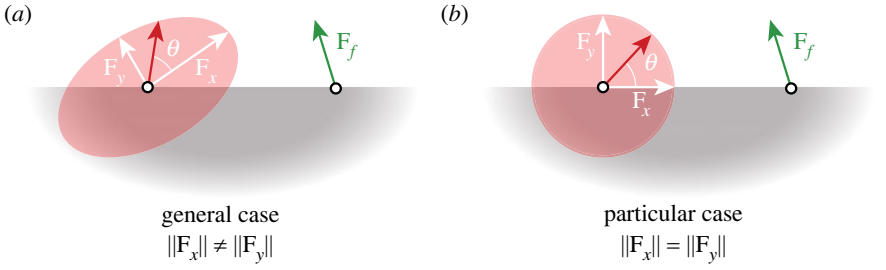

Figure 7. Schematic of the domain of possible load cases (red), the load basis vectors (white) for the varying load and the fixed load (green), for case 2. (*a*) General load basis vector, i.e. $||F_x|| \neq ||F_y||$ forming an ellipsoid domain, and (*b*) load basis vectors with the same magnitude, i.e. $||F_x|| = ||F_y||$ forming a circular domain.

inverting the direction of the loads does not alter the von Mises stress distribution. To see this, notice that, if we replace θ by $\theta' + \pi$ in equation (5.8), we obtain:

$$\sigma^v(\mathbf{z}, \theta') = \left\{t_{xy}\sin(2\theta + 2\pi) + 0.5\left[(t_{xx} - t_{yy})\cos(2\theta + 2\pi) + t_{xx} + t_{yy}\right]\right\}^{1/2} \tag{5.17}$$

but $\sin(2\theta + 2\pi) = \sin(2\theta)$ and $\cos(2\theta + 2\pi) = \cos(2\theta)$, which means that the expression in equation (5.17) is numerically equivalent to the expression in equation (5.8). This secondary range of admissible load directions is illustrated in figure 6.

(b) Case 2: planar load varying 360° plus a fixed load

In this section, we discuss the case in which we have a load varying 360°, plus a fixed load that does not vary in direction. A practical example that demonstrates the utility of this case is a bridge that is subjected to, among others, the self-weight load, which is always in the downward direction, plus the load caused by the wind, which can vary in direction. In this case, we can express the loads as:

$$\mathbf{F}(\theta) = \mathbf{F}_x\cos(\theta) + \mathbf{F}_y\sin(\theta) + \mathbf{F}_f, \tag{5.18}$$

where $\mathbf{F}_f$ is the load basis vector associated with the fixed load applied to the structure. Figure 7 displays a schematic of this load case. We can similarly define $\mathbf{U}_f = \mathbf{K}^{-1}F_f$, and $\boldsymbol{\sigma}_f = \mathbf{DBU}_f$, where $\mathbf{U}_f$ and $\boldsymbol{\sigma}_f$ are the displacement and stress component caused by the fixed load, respectively. We can then derive an expression for the von Mises stress (similar to case 1 in §5(a)):

$$\sigma^v = \left\{t_{xx}\cos^2(\theta) + t_{yy}\sin^2(\theta) + 2t_{xy}\cos(\theta)\sin(\theta) + 2t_{xf}\cos(\theta) + t_{ff} + 2t_{yf}\sin(\theta)\right\}^{1/2} \tag{5.19}$$

in which we further define the extra quadratic stress terms $t_{ff} = \boldsymbol{\sigma}_f^T\mathbf{V}\boldsymbol{\sigma}_f$, $t_{xf} = \boldsymbol{\sigma}_x^T\mathbf{V}\boldsymbol{\sigma}_f$, and $t_{yf} = \boldsymbol{\sigma}_y^T\mathbf{V}\boldsymbol{\sigma}_f$. In this form, equation (5.19) has no clear optima, so we apply the Weierstrass variable

substitution [42], also known as half-angle tangent substitution:

$$\sin(\theta) = \frac{2u}{1+u^2} \quad \text{and} \quad \cos(\theta) = \frac{1-u^2}{1+u^2}, \tag{5.20}$$

which leads to the expression:

$$\sigma^v = \left\{ \frac{1}{(u^2+1)^2} \left[(t_{xx} + t_{ff} - 2t_{xf})u^4 + 4(t_{yf} - t_{xy})u^3 \right. \right.$$
$$\left. \left. + \; 2(t_{ff} + 2t_{yy} - t_{xx})u^2 + 4(t_{yf} + t_{xy})u + t_{xx} + 2t_{xf} + t_{ff} \right] \right\}^{1/2}. \tag{5.21}$$

Now, we have to solve the related optimization problem:

$$\left.\begin{aligned} &\max_{u \in \mathrm{R}} \; [\sigma^v(\mathbf{z}, u)]^2 \\ &\text{with: } \mathbf{K}(\mathbf{z})\mathbf{U}_x = \mathbf{F}_x, \quad \mathbf{K}(\mathbf{z})\mathbf{U}_y = \mathbf{F}_y, \quad \mathbf{K}(\mathbf{z})\mathbf{U}_f = \mathbf{F}_f. \end{aligned}\right\} \tag{5.22}$$

In order to find the solution to the problem in equation (5.22), we look for the critical points by differentiating the objective function with respect to the optimization variable and finding the roots of such expression:

$$\frac{\partial(\sigma^v(\mathbf{z}, u))^2}{\partial u} = \frac{4(t_{xy} - t_{yf})u^4 + 8(t_{xx} - t_{yy} - t_{xf})u^3}{(u^2+1)^3}$$
$$+ \frac{-24t_{xy}u^2 + 8(t_{yy} - t_{xx} - t_{xf})u + 4t_{xy} + 4t_{yf}}{(u^2+1)^3} = 0. \tag{5.23}$$

Notice that the denominator is never zero, and, therefore, we can find the roots of the above expression by looking exclusively at the numerator, which is a fourth-order polynomial. The roots of a fourth-order polynomial have closed expressions based on the rationals of the polynomial. These expressions are too extensive to be displayed here, but can easily be found in literature [43,44]. Numerical experiments demonstrate that the maximum is attained at different roots depending on the values of the coefficients of the equation. Thus, we add a stress constraint for each root of equation (5.23). This means that our optimization problem will have four times the number of constraints of the original problem; however, only the constraints associated with the actual optima of the expression of the von Mises stress will be active at the optimal points, and our numerical experiments demonstrate that the AL formulation is able to accommodate the extra number of constraints without any detriment to the final solution. With this, the value for the critical von Mises stress is:

$$\widetilde{\sigma}^v = \left\{ \frac{1}{((u^\star)^2+1)^2} \left[(t_{xx} + t_{ff} - 2t_{xf})(u^\star)^4 + 4(t_{yf} - t_{xy})(u^\star)^3 \right. \right.$$
$$\left. \left. + 2(t_{ff} + 2t_{yy} - t_{xx})(u^\star)^2 + 4(t_{yf} + t_{xy})(u^\star) + t_{xx} + 2t_{xf} + t_{ff} \right] \right\}^{1/2}, \tag{5.24}$$

where $u^\star$ are the roots of the fourth degree polynomial displayed in equation (5.23). As an important side note, the polynomial in equation (5.23) might have repeated roots (i.e. a root with a multiplicity greater than 1), or even imaginary roots. The repeated roots do not pose a problem in the calculation of the constraints. However, imaginary roots do not have a clear physical meaning, and therefore, we set the value of the imaginary roots to zero in the implementation. This introduces a slight discontinuity in the sensitivity, but the optimizer seems to be able to handle this mild discontinuity.

(c) Case 3: multiple loads varying independently with different angles

In this section, we address the case in which we have several loads varying independently of each other. In this case, the variable that controls the angle of the loads, $\boldsymbol{\theta}$, is a vector in $[-\pi, \pi]^n$, where n is the number of loads, and each component of this vector controls the angle of a different load.

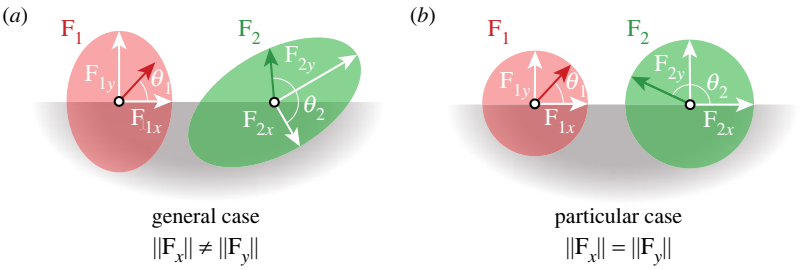

Figure 8. Schematic of the domain of possible load cases in red and green, and the load vector basis in white for case 3. (*a*) General load basis vector, i.e. $||F_{1x}|| \neq ||F_{1y}||$, and $||F_{2x}|| \neq ||F_{2y}||$ forming ellipsoid domains, and (*b*) load basis vectors with the same magnitude, i.e. $||F_{1x}|| = ||F_{1y}||$ and $||F_{2x}|| = ||F_{2y}||$ forming a circular domain.

First, we develop a solution to this problem based on the simple case of $n = 2$, i.e. two loads with two independent angles, and then we generalize the solution for an arbitrary number of loads, n. Let θ_1 and θ_2 be the first and second components of $\boldsymbol{\theta}$. Also, let $\mathbf{F}_1$ and $\mathbf{F}_2$ be the forces that vary in direction with θ_1 and θ_2, respectively. Figure 8 displays a schematic of this load case. We can write each force as the sum of linearly independent components as before:

$$\mathbf{F} = \mathbf{F_1}(\theta_1) + \mathbf{F_2}(\theta_2) \tag{5.25}$$

in which

$$\left.\begin{aligned} \mathbf{F_1}(\theta_1) &= \mathbf{F}_{1x}\cos(\theta_1) + \mathbf{F}_{1y}\sin(\theta_1) \\ \text{and} \quad \mathbf{F_2}(\theta_2) &= \mathbf{F}_{2x}\cos(\theta_2) + \mathbf{F}_{2y}\sin(\theta_2). \end{aligned}\right\} \tag{5.26}$$

We can then perform a similar derivation as in §5(a) to obtain:

$$\mathbf{U}_{1x} = (\mathbf{K}^{-1}\mathbf{F}_{1x}), \quad \mathbf{U}_{1y} = (\mathbf{K}^{-1}\mathbf{F}_{1y}),$$
$$\mathbf{U}_{2x} = (\mathbf{K}^{-1}\mathbf{F}_{2x}) \quad \text{and} \quad \mathbf{U}_{2y} = (\mathbf{K}^{-1}\mathbf{F}_{2y})$$

and the respective stresses:

$$\boldsymbol{\sigma}_{1x} = \mathbf{DBU}_{1x}, \quad \boldsymbol{\sigma}_{1y} = \mathbf{DBU}_{1y}, \quad \boldsymbol{\sigma}_{2x} = \mathbf{DBU}_{2x} \quad \text{and} \quad \boldsymbol{\sigma}_{2y} = \mathbf{DBU}_{2y}.$$

By defining the quadratic stress terms:

$$\left.\begin{aligned} t_{1xx} &= \boldsymbol{\sigma}_{1x}\mathbf{V}\boldsymbol{\sigma}_{1x} \quad t_{1yy} = \boldsymbol{\sigma}_{1y}\mathbf{V}\boldsymbol{\sigma}_{1y} \quad t_{1xy} = \boldsymbol{\sigma}_{1x}\mathbf{V}\boldsymbol{\sigma}_{1y} \\ t_{2xx} &= \boldsymbol{\sigma}_{2x}\mathbf{V}\boldsymbol{\sigma}_{2x} \quad t_{2yy} = \boldsymbol{\sigma}_{2y}\mathbf{V}\boldsymbol{\sigma}_{2y} \quad t_{2xy} = \boldsymbol{\sigma}_{2x}\mathbf{V}\boldsymbol{\sigma}_{2y} \\ \text{and} \quad s_{xx} &= \boldsymbol{\sigma}_{1x}\mathbf{V}\boldsymbol{\sigma}_{2x} \quad s_{yy} = \boldsymbol{\sigma}_{1y}\mathbf{V}\boldsymbol{\sigma}_{2y} \quad s_{xy} = \boldsymbol{\sigma}_{1x}\mathbf{V}\boldsymbol{\sigma}_{2y} \quad s_{yx} = \boldsymbol{\sigma}_{1y}\mathbf{V}\boldsymbol{\sigma}_{2x}. \end{aligned}\right\} \tag{5.27}$$

The von Mises stress can be computed as:

$$\begin{aligned} \sigma^v = \{&t_{1xx}\cos^2(\theta_1) + t_{1yy}\sin^2(\theta_1) + 2t_{1xy}\sin(\theta_1)\cos(\theta_1) \\ &+ t_{2xx}\cos^2(\theta_2) + t_{2yy}\sin^2(\theta_2) + 2t_{2xy}\sin(\theta_2)\cos(\theta_2) \\ &+ 2s_{xx}\cos(\theta_1)\cos(\theta_2) + 2s_{yy}\sin(\theta_1)\sin(\theta_2) \\ &+ 2s_{xy}\cos(\theta_1)\sin(\theta_2) + 2s_{yx}\sin(\theta_1)\cos(\theta_2)\}^{1/2}. \end{aligned} \tag{5.28}$$

We further simplify equation (5.28), using trigonometric identities, to obtain:

$$\begin{aligned} \sigma^v = \big\{&t_{1xy}\sin(2\theta_1) + 0.5\left[(t_{1xx} - t_{1yy})\cos(2\theta_1) + t_{1xx} + t_{1yy}\right] \\ &+t_{2xy}\sin(2\theta_2) + 0.5\left[(t_{2xx} - t_{2yy})\cos(2\theta_2) + t_{2xx} + t_{2yy}\right] \\ &+(s_{xy} + s_{yx})\sin(\theta_1 + \theta_2) + (s_{xx} - s_{yy})\cos(\theta_1 + \theta_2) \\ &+(s_{yx} - s_{xy})\sin(\theta_1 - \theta_2) + (s_{xx} + s_{yy})\cos(\theta_1 - \theta_2)\big\}^{1/2}. \end{aligned} \tag{5.29}$$

We then have to solve the related optimization problem:

$$\left.\begin{aligned} &\max_{\boldsymbol{\theta}\in\Gamma} [\sigma^v(\mathbf{z},\boldsymbol{\theta})]^2 \\ &\text{with: } \mathbf{K}(\mathbf{z})\mathbf{U}_{1x} = \mathbf{F}_{1x}, \quad \mathbf{K}(\mathbf{z})\mathbf{U}_{1y} = \mathbf{F}_{1y} \\ &\qquad\quad \mathbf{K}(\mathbf{z})\mathbf{U}_{2x} = \mathbf{F}_{2x}, \quad \mathbf{K}(\mathbf{z})\mathbf{U}_{2y} = \mathbf{F}_{2y}. \end{aligned}\right\} \tag{5.30}$$

Solving this optimization problem analytically would be equivalent to finding the zeros of a multivariate polynomial of sixth degree for which no analytical solution exists; however, we can obtain an analytic upper bound to worst-case stress caused by the combined loads. To obtain this upper bound, we decompose the expression of the squared von Mises stress into three parts[2] :

$$\left.\begin{aligned} \xi_1 &= t_{1xy}\sin(2\theta_1) + 0.5\left[(t_{1xx} - t_{1yy})\cos(2\theta_1) + t_{1xx} + t_{1yy}\right] \\ \xi_2 &= t_{2xy}\sin(2\theta_2) + 0.5\left[(t_{2xx} - t_{2yy})\cos(2\theta_2) + t_{2xx} + t_{2yy}\right] \\ \text{and} \quad \xi_{12} &= (s_{xy} + s_{yx})\sin(\theta_1 + \theta_2) + (s_{xx} - s_{yy})\cos(\theta_1 + \theta_2) \\ &\quad + (s_{yx} - s_{xy})\sin(\theta_1 - \theta_2) + (s_{xx} + s_{yy})\cos(\theta_1 - \theta_2) \end{aligned}\right\} \tag{5.31}$$

The maximum of the sum of these terms is less than or equal to the sum of the maximum of each term. Therefore, we compute the maximum of each term and use the sum of the three terms as an upper bound on the critical stress. The expressions for ξ_1 and ξ_2 resemble equation (5.9), which we have already derived a solution for. Thus, we have:

$$\left.\begin{aligned} \xi_1^\star &= t_{1xy}\sin(2\theta_1^\star) + 0.5\left[(t_{1xx} - t_{1yy})\cos(2\theta_1^\star) + t_{1xx} + t_{1yy}\right] \\ \text{and} \quad \xi^\star &= t_{2xy}\sin(2\theta_2^\star) + 0.5\left[(t_{2xx} - t_{2yy})\cos(2\theta_2^\star) + t_{2xx} + t_{2yy}\right] \end{aligned}\right\} \tag{5.32}$$

with:

$$\theta_1^\star = \frac{1}{2}\tan^{-1}(2t_{1xy}, t_{1xx} - t_{1yy}) \quad \text{and} \quad \theta_2^\star = \frac{1}{2}\tan^{-1}(2t_{2xy}, t_{2xx} - t_{2yy}). \tag{5.33}$$

To find a solution for the ξ_{12} term, we substitute $u = \theta_1 + \theta_2$ and $v = \theta_1 - \theta_2$ into the expression for ξ_{12} in equation (5.32), and separate ξ_{12} in two terms, $\xi_{12u} + \xi_{12v}$, each containing only terms with u, or v:

$$\left.\begin{aligned} \xi_{12u} &= (s_{xy} + s_{yx})\sin(u) + (s_{xx} - s_{yy})\cos(u) \\ \text{and} \quad \xi_{12v} &= (s_{yx} - s_{xy})\sin(v) + (s_{xx} + s_{yy})\cos(v). \end{aligned}\right\} \tag{5.34}$$

Differentiating the expressions in equation (5.34) and setting them equal to zero, we find the following critical points:

$$\left.\begin{aligned} u^{\mathrm{cr}} &= \begin{cases} \tan^{-1}(s_{xy} + s_{yx}, s_{xx} - s_{yy}) \\ \tan^{-1}(-(s_{xy} + s_{yx}), -(s_{xx} - s_{yy})) \end{cases} \\ \text{and} \quad v^{\mathrm{cr}} &= \begin{cases} \tan^{-1}(s_{yx} - s_{xy}, s_{xx} + s_{yy}) \\ \tan^{-1}(-(s_{yx} - s_{xy}), -(s_{xx} + s_{yy})). \end{cases} \end{aligned}\right\} \tag{5.35}$$

We denote the first solutions in equation (5.35) $u^{\mathrm{cr}}_{\max}$ and $v^{\mathrm{cr}}_{\max}$ and the second solutions $u^{\mathrm{cr}}_{\min}$ and $v^{\mathrm{cr}}_{\min}$. By taking second derivatives with respect to u and v and evaluating them at the critical

[2]Again, we square the von Mises stress in the objective function to eliminate the square root on the right-hand side, because it does not influence the solution of the optimization problem.

points, we find:

$$\left.\frac{\partial^2 \xi_{12}}{\partial u^2}\right|_{u=u^{\mathrm{cr}}_{\max}} = -\left\{(s_{xy}+s_{yx})^2+(s_{xx}-s_{yy})^2\right\}^{1/2} \tag{5.36}$$

$$\left.\frac{\partial^2 \xi_{12}}{\partial u^2}\right|_{u=u^{\mathrm{cr}}_{\min}} = \left\{(s_{xy}+s_{yx})^2+(s_{xx}-s_{yy})^2\right\}^{1/2} \tag{5.37}$$

$$\left.\frac{\partial^2 \xi_{12}}{\partial v^2}\right|_{v=v^{\mathrm{cr}}_{\max}} = -\left\{(s_{xy}-s_{yx})^2+(s_{xx}+s_{yy})^2\right\}^{1/2} \tag{5.38}$$

and

$$\left.\frac{\partial^2 \xi_{12}}{\partial v^2}\right|_{v=v^{\mathrm{cr}}_{\min}} = \left\{(s_{xy}-s_{yx})^2+(s_{xx}+s_{yy})^2\right\}^{1/2}. \tag{5.39}$$

The second derivatives of ξ_{12} with respect to u and v are always non-positive at $u=u^{\mathrm{cr}}_{\max}$ and $v=v^{\mathrm{cr}}_{\max}$ and always non-negative at $u=u^{\mathrm{cr}}_{\min}$ and $v=v^{\mathrm{cr}}_{\min}$, meaning that the point $(u^{\mathrm{cr}}_{\max}, v^{\mathrm{cr}}_{\max})$ is a local maximum, $(u^{\mathrm{cr}}_{\min}, v^{\mathrm{cr}}_{\min})$ is a local minimum, and $(u^{\mathrm{cr}}_{\max}, v^{\mathrm{cr}}_{\min})$ and $(u^{\mathrm{cr}}_{\min}, v^{\mathrm{cr}}_{\max})$ are saddle points. Since these are the only critical points in the domain and the function is smooth and periodic, $(u^{\mathrm{cr}}_{\max}, v^{\mathrm{cr}}_{\max})$ is the global maximum and $(u^{\mathrm{cr}}_{\min}, v^{\mathrm{cr}}_{\min})$ is the global minimum. Therefore, the maximum of ξ_{12}:

$$u^\star = \tan^{-1}(s_{xy}+s_{yx}, s_{xx}-s_{yy}) \quad \text{and} \quad v^\star = \tan^{-1}(s_{yx}-s_{xy}, s_{xx}+s_{yy}) \tag{5.40}$$

and the maximum is:

$$\xi^\star_{12} = (s_{xy}+s_{yx})\sin(u^\star)+(s_{xx}-s_{yy})\cos(u^\star)+(s_{yx}-s_{xy})\sin(v^\star)+(s_{xx}+s_{yy})\cos(v^\star). \tag{5.41}$$

To obtain the upper limit, $\widehat{\sigma}^v$, for $\widetilde{\sigma}^v$, we sum $\xi^\star_1$, $\xi^\star_2$ and $\xi^\star_{12}$:

$$\widehat{\sigma}^v = \{\xi^\star_1+\xi^\star_2+\xi^\star_{12}\}^{1/2}. \tag{5.42}$$

By using the upper limit, $\widehat{\sigma}^v$, in the stress constraints, we can guarantee that the stress will be below the limit for any of the possible load directions.

(i) Limiting the range of θ_1 and θ_2

If we want to restrict the range of one, or both load angles, we can do so by restricting each expression in equation (5.31) individually, and applying the solution presented in §5(a). Furthermore, we can construct the admissible range for u and v based on θ_{1r} and θ_{2r} as $[-(\theta_{1r}+\theta_{2r}), (\theta_{1r}+\theta_{2r})]$ for both u and v, in which $[-\theta_{1r}, \theta_{1r}]$ and $[-\theta_{2r}, \theta_{2r}]$ are the ranges of admissible angles for θ_1 and θ_2, respectively. With these limited ranges, we have:

$$\left.\begin{aligned}
\theta^\star_1 &= \min\left\{\max\left[\frac{1}{2}\tan^{-1}(2t_{1xy}, t_{1xx}-t_{1yy}), -\theta_{1r}\right], \theta_{1r}\right\}\\
\theta^\star_2 &= \min\left\{\max\left[\frac{1}{2}\tan^{-1}(2t_{2xy}, t_{2xx}-t_{2yy}), -\theta_{2r}\right], \theta_{2r}\right\}\\
u^\star &= \min\left\{\max[\tan^{-1}(s_{xy}+s_{yx}, s_{xx}-s_{yy}), -(\theta_{1r}+\theta_{2r})], (\theta_{1r}+\theta_{2r})\right\}\\
\text{and}\quad v^\star &= \min\left\{\max[\tan^{-1}(s_{yx}-s_{xy}, s_{xx}+s_{yy}), -(\theta_{1r}+\theta_{2r})], (\theta_{1r}+\theta_{2r})\right\}.
\end{aligned}\right\} \tag{5.43}$$

(ii) Error analysis of critical stress upper bound

The use of an upper bound on the worst-case stress constraint leads to an overestimation of the actual maximum stress caused on the structure by the loads. This overestimation of the stress can lead to an over design, resulting in structures that have extra unnecessary material. Therefore, the more accurate this upper bound is, i.e. the closer it is to the actual worst-case stress, the less extra unnecessary material the optimal structure will have. To evaluate the accuracy of such an upper

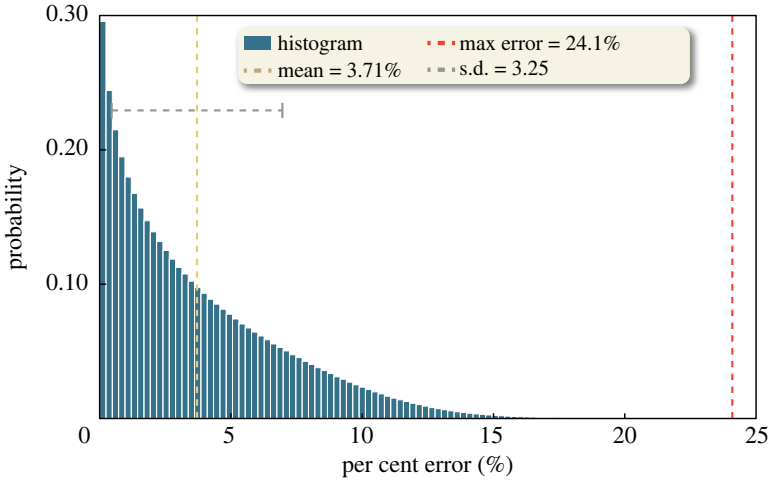

Figure 9. Histogram generated using a sample of 100 million uniformly distributed random stress basis vectors representing the underlying probability distribution of the percent error (see equation (5.44)) between the proposed upper bound, and the worst-case stress.

bound, we generated a sample of 100 million uniformly distributed random stress basis vectors $(\boldsymbol{\sigma}_{1x}, \boldsymbol{\sigma}_{1y}, \boldsymbol{\sigma}_{2x}, \boldsymbol{\sigma}_{2y})$, and computed a percent error (see equation (5.44)) comparing the worst-case stress with the proposed upper bound using these random stress basis vectors. The result of such statistical analysis of the error is displayed in figure 9 in the form of a histogram. In this histogram, we see that the mean error was 3.71% with a 3.25 standard deviation, and that the maximum percent error was 24.1%. We also notice that this probability distribution is skewed to the left, indicating that the error rarely attains values close to this maximum error. With this analysis, we show that the percent error is moderate, and that the proposed upper bound is significantly accurate.

To verify that this sample of 100 million random stress basis vectors is representative of the underlying probability distribution, we performed a numerical convergence analysis by starting with a sample of 10 million and increasing its size, 10 million by 10 million, until we reached the 100 million sample size. We also generated 10 different samples of 100 million elements, which proved to be numerically identical. With these two numerical experiments, we guaranteed that the sample size used was large enough to provide us with a trustworthy representation of the underlying probability distribution.

$$\text{Percent Error (\%)} = \left| \frac{\{\xi_1^\star + \xi_2^\star + \xi_{12}^\star\}^{1/2} - \sigma_{cr}^v}{\sigma_{cr}^v} \right| \times 100 \tag{5.44}$$

in which $\{\xi_1^\star + \xi_2^\star + \xi_{12}^\star\}^{1/2}$ is the proposed upper bound for the worst-case stress, and σ_{cr}^v is the worst-case stress.

(iii) Generalization to more than two independent loads

To generalize this approach for an arbitrary number of loads represented by an arbitrary number of angles θ_i, notice that the interactions between the loads in equation (5.28) occur pairwise, because the expression of the von Mises stress is bilinear. Therefore, we can obtain a similar estimation for the upper bound of the von Mises stress by separating the terms that depend exclusively on θ_i and the cross terms between θ_i and θ_j for $i \neq j$, and then summing them all together. Equation (5.45) displays this approach for a general number n of angles θ_i, in which the

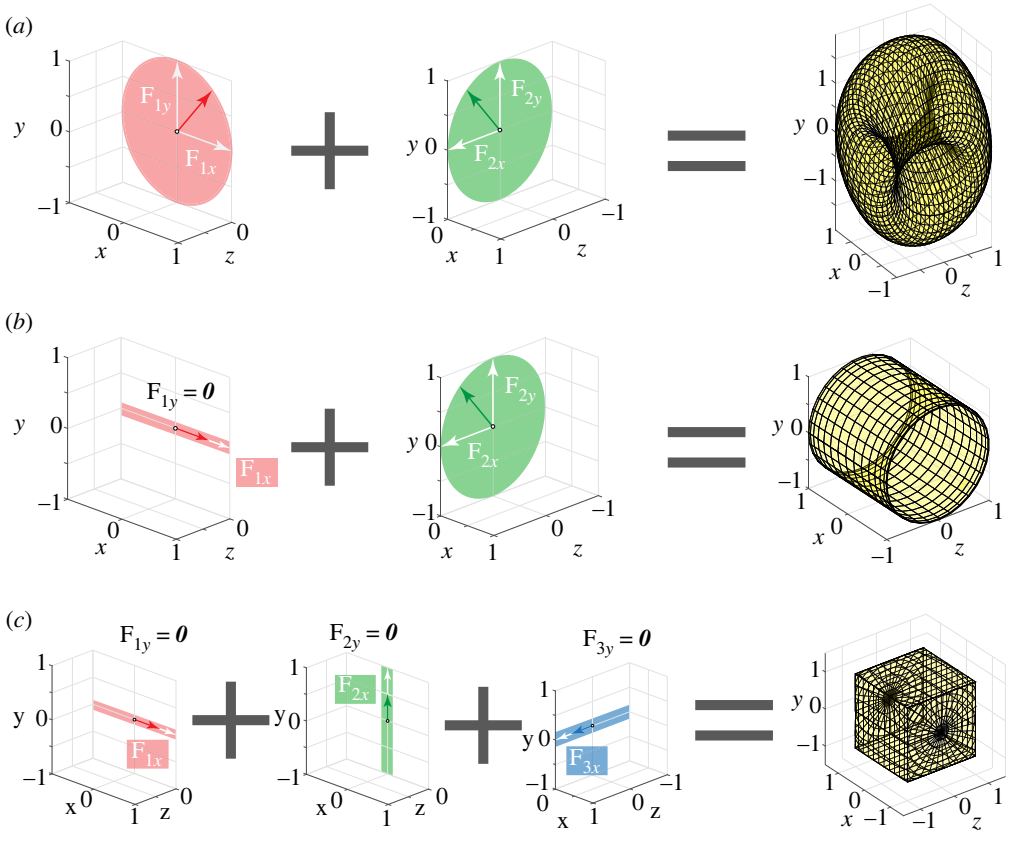

Figure 10. Schematic of how to combine loads with independently varying angles to achieve a load that varies in three dimensions.

terms ξ_i and ξ_{ij} are expressed in equation (5.31) by replacing the appropriate indexes.

$$\widehat{\sigma}^v = \left\{ \sum_{i=1}^{n} \left(\xi_i + \sum_{j=i+1}^{n} \xi_{ij} \right) \right\}^{1/2} \tag{5.45}$$

(d) Case 4: load varying in three dimensions

The last case presented in this work is for three-dimensional problems in which the loads can vary, not only in a plane, but also in out-of-plane directions, representing a whole surface of possible load directions. To account for these out-of-plane load components, we combine two loads varying independently in direction (with θ_1 and θ_2), with the appropriate basis, using the derivations of case 3. As seen in figure 10*a*, by combining two independent loads with bases that form orthogonal planes, we obtain a three-dimensional load surface that accounts for out-of-plane load components. Furthermore, by combining independent loads of different forms we can obtain different three-dimensional load surfaces (figure 10*b*,*c*). Notice that, by setting one of the bases (F_y) to zero in figure 10*b*,*c*, we obtain a load that only varies in intensity, from $-F_x$ to F_x, in a fixed direction.

6. Generalization of load decomposition and varying load intensity

All of the methodology developed in the previous section is based on decomposing the load into load basis vectors that we can use to obtain upper limits on the worst-case von Mises

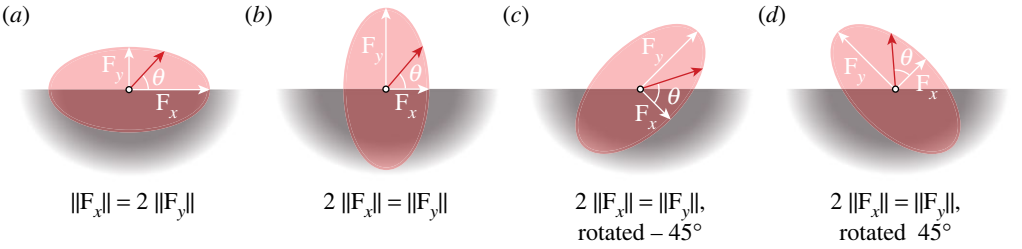

Figure 11. Load case 1 with different magnitudes and different orientations for the load basis vectors F_x and F_y.

stress. However, no assumption was made about the direction or magnitude of these basis vectors. Consequently, the previously obtained solutions are valid even if F_x and F_y have different magnitudes, or if F_x and F_y are not aligned with the x- and y-axes. If we change the magnitude of F_x in relation to F_y, we obtain a domain of load cases that forms an ellipse instead of a circle, as displayed in figure 11*a*,*b*. We can also rotate this ellipse by rotating the basis vectors, as displayed in figure 11*c*,*d*.[3] This freedom to choose the load basis vectors provides extra flexibility, making it possible for the designer to define load cases in which a specific load direction is more relevant than the other.

7. Topology optimization formulation

The general formulation proposed in this work considering continuously varying load is presented here in equation (7.1):

$$\left.\begin{aligned} &\min_{\mathbf{z}} M(\mathbf{z}) = \sum_{e=1}^{N_e} \tilde{\rho}_e v_e \\ &\text{s.t.: } g_j(\mathbf{z}, \widehat{\sigma}^v(\boldsymbol{\theta}^\star)) \le 0, \quad j = 1, \ldots, N_c \\ &\qquad 0 \le z_e \le 1, \quad e = 1, \ldots, N_e \\ &\text{with: } \mathbf{K}(\mathbf{z})\mathbf{U}_{ix} = \mathbf{F}_{ix} \quad \mathbf{K}(\mathbf{z})\mathbf{U}_{iy} = \mathbf{F}_{iy}, \quad i = 1, \ldots, n \\ &\qquad \mathbf{K}(\mathbf{z})\mathbf{U}_f = \mathbf{F}_f \\ &\qquad \boldsymbol{\theta}^\star = \boldsymbol{\theta}(\mathbf{U}_{1x}, \ldots, \mathbf{U}_{nx}, \mathbf{U}_{1y}, \ldots, \mathbf{U}_{ny}, \mathbf{U}_f) \\ &\qquad \tilde{\rho}(\mathbf{z}) = \mathcal{H}(\mathbf{P}\mathbf{z}) \end{aligned}\right\} \tag{7.1}$$

in which the equation for the worst-case von Mises stress $\widehat{\sigma}^v(\boldsymbol{\theta}^\star)$ is given by either equation (5.8), or (5.24), or (5.45), which itself is a function of the worst-case load angle $\boldsymbol{\theta}^\star$ given by either equation (5.16), or (5.23), or (5.43), depending on whether we are using case 1, or 2, or 3, respectively (note that case 4 is a particular instance of case 3). The worst-case load angle $\boldsymbol{\theta}^\star$ is formulated as a function of the displacement components, $(\mathbf{U}_{1x}, \ldots, \mathbf{U}_{nx}, \mathbf{U}_{1y}, \ldots, \mathbf{U}_{ny}, \mathbf{U}_f)$, obtained through the solution of the equilibrium equations with their respective load basis vectors, $(\mathbf{F}_{1x}, \ldots, \mathbf{F}_{nx}, \mathbf{F}_{1y}, \ldots, \mathbf{F}_{ny}, \mathbf{F}_f)$. If we are in case 1, the number of loads, n, is one, otherwise, if we are in case 3 the number of loads is defined by the problem (i.e. the number of independent varying loads). If we are in case 1, or case 3 the terms associated with the fixed load are equal to zero, $\mathbf{U}_f = \mathbf{F}_f = \mathbf{0}$, and the equation is null, otherwise, if we are in case 2, the terms $\mathbf{F}_f$ and $\mathbf{U}_f$ are defined by the fixed load, and its displacement according to the problem. To solve the optimization problem described in equation (7.1), we use the AL method (as described in §3) in which we solve a sequence of (k) optimization problems, given by equation (7.2), and the solution

[3]We use this property in case 2 (§5(a)) to shift the range of admissible angles to be centred around the origin.

of these sub-problems, obtained by implementing the optimization algorithm presented in §S2, converges to the solution of the original problem (for more detail see [2]).

$$\left.\begin{aligned}
&\min_{\mathbf{z}} J^{(k)}(\mathbf{z}) = \sum_{e=1}^{N_e} \tilde{\rho}_e v_e + \eta \sum_{j=1}^{N_c} \left[\lambda_j^{(k)} h_j(\mathbf{z}, \widehat{\sigma}^v(\boldsymbol{\theta}^\star)) + \frac{\mu^{(k)}}{2} h_j(\mathbf{z}, \widehat{\sigma}^v(\boldsymbol{\theta}^\star))^2 \right] \\
&\text{s.t.: } 0 \le z_e \le 1, \quad e = 1, \ldots, N_e \\
&\text{with: } \mathbf{K}(\mathbf{z})\mathbf{U}_{ix} = \mathbf{F}_{ix} \quad \mathbf{K}(\mathbf{z})\mathbf{U}_{iy} = \mathbf{F}_{iy}, \quad i = 1, \ldots, n \\
&\qquad \mathbf{K}(\mathbf{z})\mathbf{U}_f = \mathbf{F}_f \\
&\qquad \boldsymbol{\theta}^\star = \boldsymbol{\theta}(\mathbf{U}_{1x}, \ldots, \mathbf{U}_{nx}, \mathbf{U}_{1y}, \ldots, \mathbf{U}_{ny}, \mathbf{U}_f) \\
&\qquad \tilde{\rho}(\mathbf{z}) = \mathcal{H}(\mathbf{P}\mathbf{z}) \\
&\qquad h_j(\mathbf{z}, \widehat{\sigma}^v(\boldsymbol{\theta}^\star)) = \max \left[g_j(\mathbf{z}, \widehat{\sigma}^v(\boldsymbol{\theta}^\star)), \frac{-\lambda_j^{(k)}}{\mu^{(k)}} \right]
\end{aligned}\right\} \tag{7.2}$$

8. Numerical results

This section presents numerical results obtained through an implementation of the formulations to handle continuously varying load cases described in this work.[4] The numerical results presented here, which consist of the two-dimensional double L-bracket, and the three-dimensional bracket from the General Electric (GE) jet engine bracket challenge,[5] verify the effectiveness of the proposed formulation. For more details on the implementation see SS1 of the electronic supplementary material.

(a) Double L-bracket

In this section, we present the results obtained for the double L-bracket domain, displayed in figure 12*a*, considering two loads varying simultaneously with the same angle (case 1, §5(a), one fixed load and one load varying in angle (case 2, §5(b)), and two loads varying independently of each other (case 3, §5(c)). The numerical parameters for this problem are displayed in table 2. In figure 12*b*, we display the solution obtained for a fixed downward load (i.e. $\theta_1 = \theta_2 = \theta = -90^\circ$) to serve as a base for comparison with the other load cases. We also use this solution to exemplify the importance of considering multiple load directions in the design. In figure 12*g*, we display this solution's maximum stress as we vary the load angle. Notice that the stress limit is only satisfied for the angle $\theta = -90^\circ$ that was considered during the optimization, and for the angle $\theta = -90^\circ + 180^\circ = 90^\circ$.[6] Furthermore, the plot shows that small changes in the load angle cause a drastic increase in the maximum stress meaning that this structure is highly susceptible to failure due to small deviations in the load direction.

Figure 12*d–f* displays the optimized designs obtained for the double L-bracket considering the two loads (F_1 and F_2) varying with the same angle $\theta_1 = \theta_2 = \theta$ for different ranges of admissible angle (θ_r), which corresponds to case 1 presented in §5(a). We can see that, as we increase the range of admissible angles, we obtain designs with more material, and greater complexity. To verify that the structure can withstand the load directions considered in the optimization, we plot, in figure 12*g*, the maximum stress of each design as we vary the load direction. We can see that the design that considers a single load direction ($\theta_r = 0$), experiences a drastic increase in the

[4]The two-dimensional numerical results were obtained through a Matlab implementation, and the three-dimensional numerical results were obtained through a C++/CUDA implementation. The hardware used to run these problems consists of a computer with an i7-4930k CPU at 3.40 GHz and 64 GB of RAM and a NVIDIA GEFORCE GTX 1080 Ti GPU running on a 64-bit operating system.

[5]https://grabcad.com/challenges/ge-jet-engine-bracket-challenge.

[6]The angle $\theta = 90^\circ$ satisfies the stress limit because of the linearity of the equilibrium equations and the symmetry of von Mises stress formulation, as explained in §5(i), which is also the reason for the symmetry of the plot.

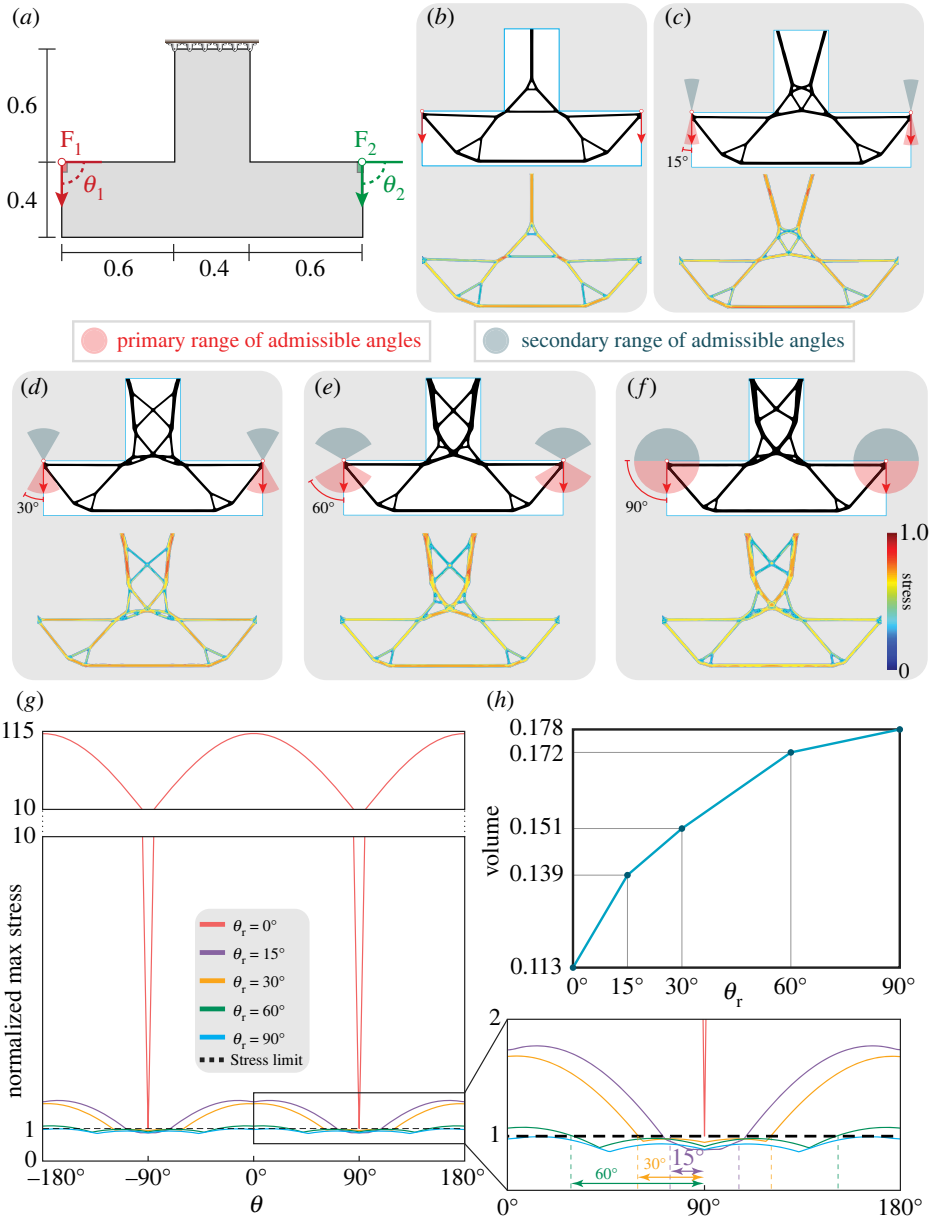

Figure 12. Double L-bracket numerical example. (*a*) Double L-bracket domain geometry and boundary conditions; (*b*) optimized design and stress map for a fixed downward load (i.e. $\theta_1 = \theta_2 = \theta = -90^\circ$); (*c*)–(*f*) optimized design and stress maps considering the two loads (F_1 and F_2) varying with the same angle $\theta_1 = \theta_2 = \theta$ for different ranges of admissible angle (θ_r), which corresponds to case 1 presented in §5(a); (*g*) maximum stress of the optimized designs in (*b*)–(*f*), as we vary the load angle; (*h*) volume fraction of the optimized designs in (*b*)–(*f*) with respect to the range of admissible load angles (θ_r) considered in the optimization.

maximum stress as we vary the load angle θ. On the other hand, by imposing a limit angle as low as 15°, we reduce the peak of maximum stress outside the admissible range. We also plot the volume fraction of each design as we increase the range of admissible load angles θ_r (figure 12*h*). As expected, the volume fraction increases as we increase the value of θ_r, because of the extra structural complexity necessary to accommodate the additional load directions.

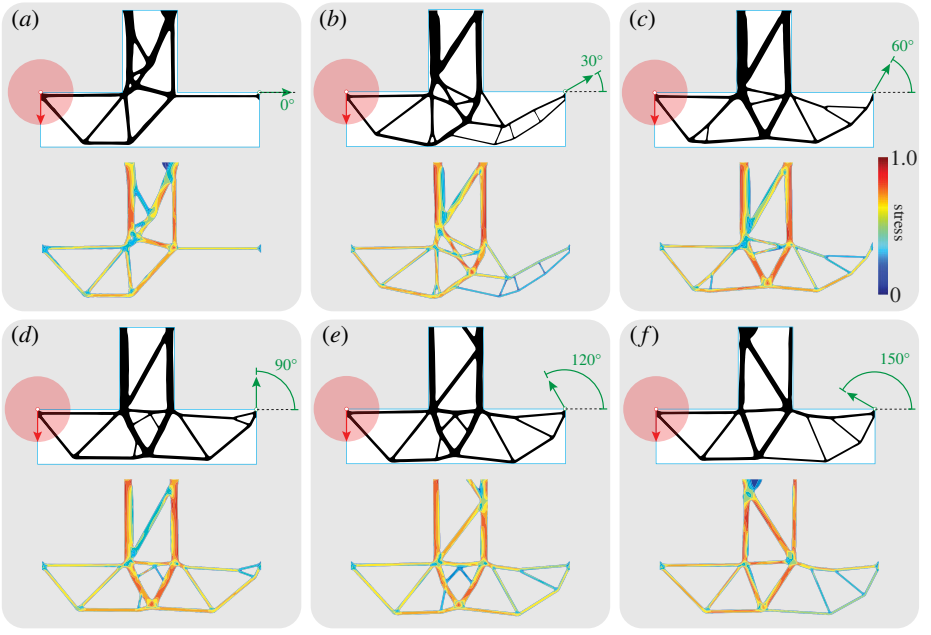

Figure 13. Double L-bracket considering one load (F_1) varying in direction with angle θ_1 combined with a simultaneous fixed load (F_2), which corresponds to case 2 presented in §5(b). (*a*)–(*f*) Optimized designs and stress map envelopes for different angles of the fixed load θ_2.

Table 2. Input parameters for the two-dimensional double L-bracket problem.

parameter	description	value
E_0	Young's modulus	1 Pa
ν	Poisson's ratio	0.3
σ_{lim}	stress limit	120 Pa
F_1	applied load	1 N
F_2	applied load	1 N
r	filter radius	0.015 m
–	load distribution length	0.06 m
–	mesh Q4 elements	220 000

Table 3. Volume fractions for the double L-beam designs of figure 13, considering a load varying in direction and a fixed load with different angles.

	fixed angle					
	0°	30°	60°	90°	120°	150°
volume fraction	0.194	0.220	0.240	0.239	0.227	0.197

Figure 13 displays the design obtained for the double L-bracket considering one load (F_1) varying in direction with angle θ_1 combined with a simultaneous fixed load (F_2), which corresponds to case 2 presented in §5(b). We can see that the results present a clear asymmetry regarding the vertical centre line, caused by the different load conditions on each side of the double L-bracket. We also display the volume fraction of each design in table 3. We choose to

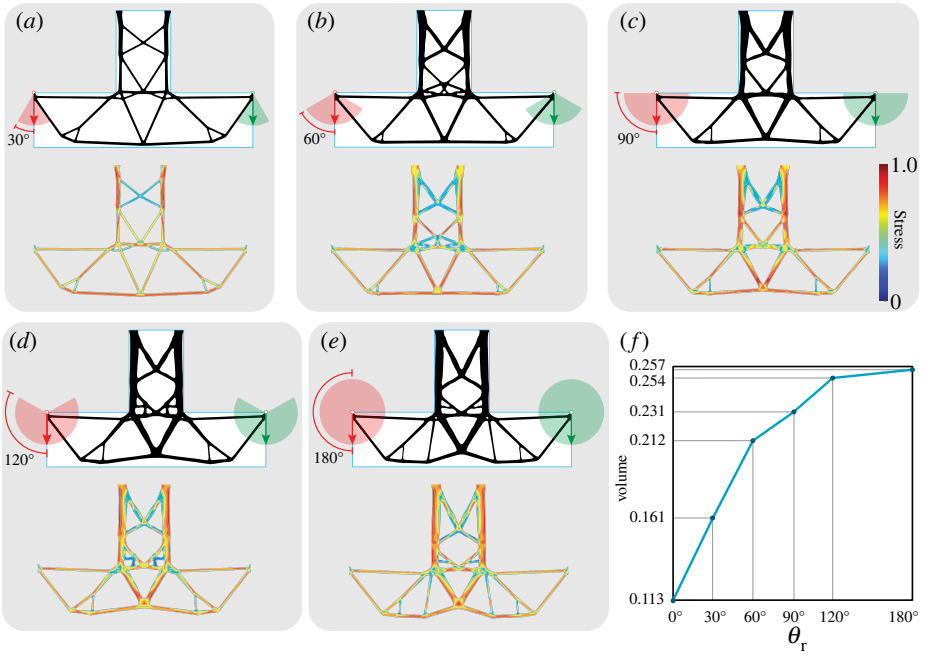

Figure 14. Double L-bracket considering two loads (F_1 and F_2) varying independently in direction with angles θ_1 and θ_2, which corresponds to case 3 presented in §5(c). (*a–e*) Optimized designs and stress map envelopes for different ranges of admissible angles; (*f*) volume fraction of the optimized designs in (*a–e*) with respect to the range of admissible load angles (θ_r) considered in the optimization.

display the volume in a table, instead of a plot, as we did for the other cases, because, for this case, we do not have a clear progression of volume, since we vary the fixed load direction, and not the range of admissible angles.

Figure 14 displays the design obtained for the double L-bracket considering two loads (F_1 and F_2) varying independently in direction with angles θ_1 and θ_2, which corresponds to case 3 presented in §5(c). This combination of loads generates designs that are completely different from the designs in figure 12, in which the loads vary with the same angle. The difference in design demonstrates the influence of this load case. We also display, in figure 14*f*, the volume fraction of the final structure in regards to the range of admissible angles, and we can see a trend of increasing volume fraction as we increase the range of angles considered in the optimization, as expected.

(b) GE jet engine bracket challenge

In this section, we present the results obtained for the GE Jet Engine Bracket Challenge domain, displayed in figure 15*a*. The domain is subjected to a load case that can vary three-dimensionally, obtained using the combination of two load cases varying independently, contained in perpendicular planes. The numerical parameters for this problem are displayed in table 4. Figure 15*c–g* displays the solutions as we gradually increase the range of admissible load directions from 0° to 15°, 30°, 60° and 90°. As we increase the load angle range, we obtain solutions with more volume distributed in a shell-like structure to withstand the extra load directions. The volume fractions of the structures are displayed in figure 15*b*, where we see the expected trend of increasing volume with the increase in the range of admissible angles.

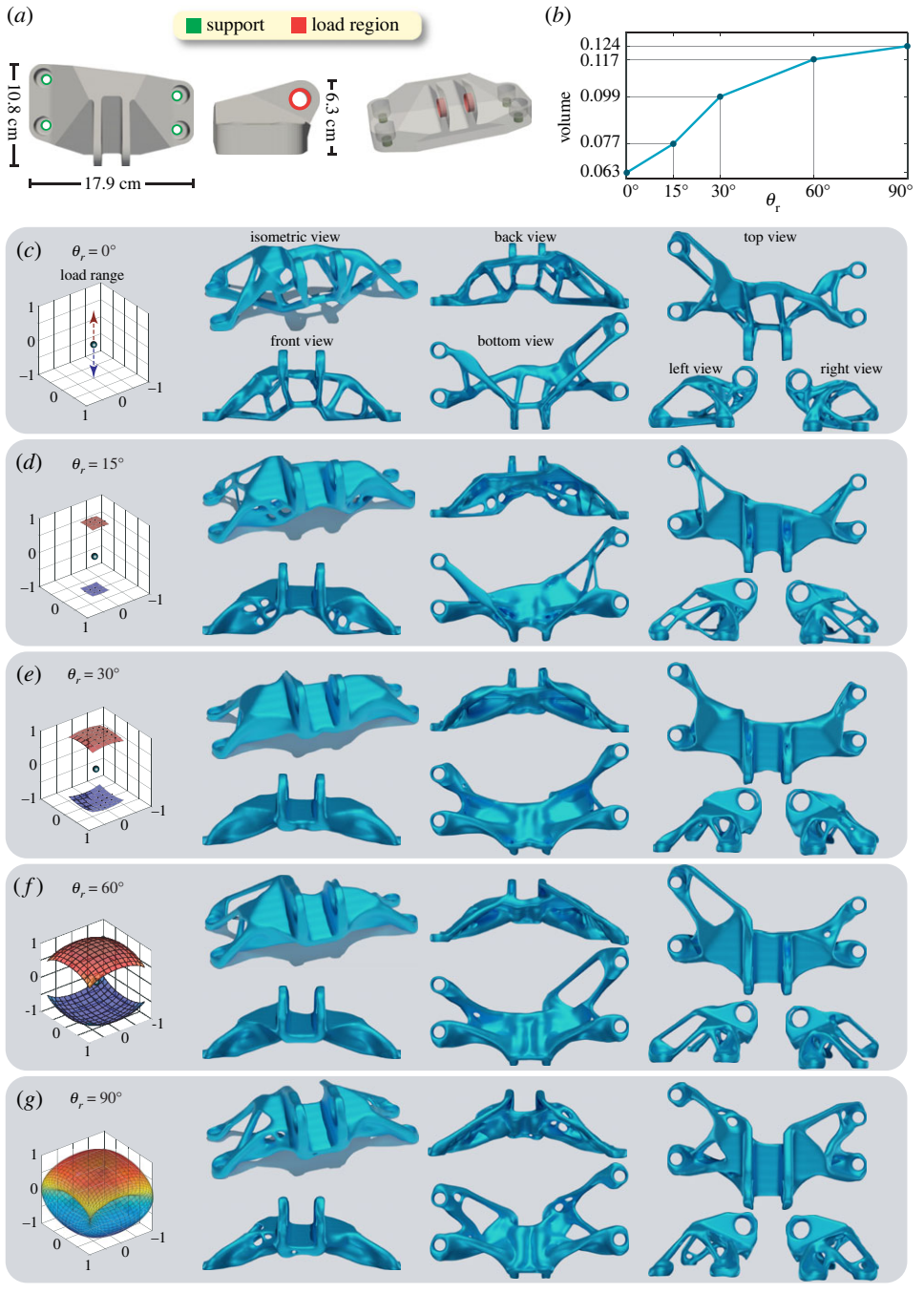

Figure 15. GE jet engine challenge problem; (*a*) design domain with the red regions indicating loading, and green regions indicating support. (*b*) Volume fraction of the GE jet engine challenge problem solutions displayed in (*c–g*) as we vary the load angle range, θ_r. (*c–g*) Isometric, top and bottom view, of the optimized structures considering 0°, 15°, 30°, 60° and 90° load angle range.

9. Concluding remarks

This paper presents an efficient and consistent technique to consider a continuous range of load angles in the topology optimization procedure with local stress constraints. The technique is

Table 4. Input parameters for the three-dimensional GE Jet Engine Bracket Challenge problem.

parameter	description	value
E_0	Young's modulus	1 Pa
ν	Poisson's ratio	0.25
σ_{lim}	stress limit	2.5 Pa
F_1	applied load	100 N
F_2	applied load	100 N
r	filter radius	2.5
–	mesh size (hexahedral elements)	3 727 159

based on a worst-case scenario approach, in which we find analytical solutions that bound the maximum stress caused by a range of admissible load angles. We developed analytical solutions for:

— a planar load varying in an arbitrary range of angles;
— a load varying in direction plus a fixed load;
— two or more loads varying independently in direction;
— a load varying in three dimensions in an arbitrary range of angles.

The technique is extremely flexible, supporting a wide variety of load conditions, including loads that vary in intensity. This wide variety of load conditions provides engineers with the tools to design structures that are a better fit for practical requirements. As demonstrated by the numerical examples, designs optimized considering only one fixed load are extremely sensitive to variations in the load angle, and small variations in the load direction, which are common in real-life situations, can cause severely high stresses, meaning that the structure might fail in practice. On the other hand, considering a range of load angles, instead of a single fixed load, leads to significantly different optimized structures that are closer to realistic engineering components, and are robust under variations of the load direction. Additionally, the technique developed here can be used for any TO problem with objective, and/or constraint functions that have a primarily bi-linear form (such as compliance), and linear state equations (see §S5 of the electronic supplementary material for a compliance minimization formulation).

Data accessibility. The code supporting this article has been uploaded as part of the electronic supplementary material.

The data are provided in electronic supplementary material [45].

Authors' contributions. F.V.S.: conceptualization, formal analysis, investigation, methodology, software, validation, visualization, writing—original draft, writing—review and editing; I.F.M.M.: conceptualization, writing—review and editing; G.H.P.: conceptualization, methodology, supervision, writing—review and editing, funding acquisition, resources.

All authors gave final approval for publication and agreed to be held accountable for the work performed therein.

Conflict of interest declaration. We declare we have no competing interests.

Funding. The research was supported by the National Science Foundation (NSF) through grant No. 2105811. F.V.S. and I.F.M.M. acknowledge the support provided by the Brazilian agencies CNPq, FAPERJ, and Coordenação de Aperfeiçoamento de Pessoal de Nível Superior—Brasil (CAPES)—Finance Code 001, and Tecgraf/PUC-Rio (Institute of Technical-Scientific Software Development).

Acknowledgements. We thank Dr Emily Sanders and Dr. Jonathan Russ for their invaluable help with the manuscript, and Dr Hugo Bastos de Sá Bruno for the insightful discussions about continuum mechanics.

References

1. Sarkisian M. 2012 *Designing tall buildings: structure as architecture*, pp. 1–208. London, UK: Routledge.
2. Senhora FV, Giraldo-Londono O, Menezes IF, Paulino GH. 2020 Topology optimization with local stress constraints: a stress aggregation-free approach. *Struct. Multidiscip. Optim.* **62**, 1639–1668. (doi:10.1007/s00158-020-02573-9)
3. Díaz AR, Bendsøe MP. 1992 Shape optimization of structures for multiple loading conditions using a homogenization method. *Struct. Optim.* **4**, 17–22. (doi:10.1007/BF01894077)
4. Lopes CG, dos Santos RB, Novotny AA. 2015 Topological derivative-based topology optimization of structures subject to multiple load-cases. *Lat. Am. J. Solids Struct.* **12**, 834–860. (doi:10.1590/1679-78251252)
5. Picelli R, Townsend S, Brampton C, Norato J, Kim HA. 2018 Stress-based shape and topology optimization with the level set method. *Comput. Methods Appl. Mech. Eng.* **329**, 1–23. (doi:10.1016/j.cma.2017.09.001)
6. Lee E, James KA, Martins JRRA. 2012 Stress-constrained topology optimization with design-dependent loading. *Struct. Multidiscip. Optim.* **46**, 647–661. (doi:10.1007/s00158-012-0780-x)
7. Ben-Tal A, Nemirovski A. 2002 Robust optimization—methodology and applications. *Math. Program.* **92**, 453–480. (doi:10.1007/s101070100286)
8. Thore CJ, Holmberg E, Klarbring A. 2017 A general framework for robust topology optimization under load-uncertainty including stress constraints. *Comput. Methods Appl. Mech. Eng.* **319**, 1–18. (doi:10.1016/j.cma.2017.02.015)
9. Guest JK, Igusa T. 2008 Structural optimization under uncertain loads and nodal locations. *Comput. Methods Appl. Mech. Eng.* **198**, 116–124. (doi:10.1016/j.cma.2008.04.009)
10. Guo X, Zhang W, Zhang L. 2013 Robust structural topology optimization considering boundary uncertainties. *Comput. Methods Appl. Mech. Eng.* **253**, 356–368. (doi:10.1016/j.cma.2012.09.005)
11. Liu J, Wen G. 2018 Continuum topology optimization considering uncertainties in load locations based on the cloud model. *Eng. Optim.* **50**, 1041–1060. (doi:10.1080/0305215X.2017.1361417)
12. Jalalpour M, Guest JK, Igusa T. 2013 Reliability-based topology optimization of trusses with stochastic stiffness. *Struct. Saf.* **43**, 41–49. (doi:10.1016/j.strusafe.2013.02.003)
13. Zhang W, Kang Z. 2017 Robust shape and topology optimization considering geometric uncertainties with stochastic level set perturbation. *Int. J. Numer. Methods Eng.* **110**, 31–56. (doi:10.1002/nme.5344)
14. Tootkaboni M, Asadpoure A, Guest JK. 2012 Topology optimization of continuum structures under uncertainty—a polynomial chaos approach. *Comput. Methods Appl. Mech. Eng.* **201–204**, 263–275. (doi:10.1016/j.cma.2011.09.009)
15. Asadpoure A, Tootkaboni M, Guest JK. 2011 Robust topology optimization of structures with uncertainties in stiffness—application to truss structures. *Comput. Struct.* **89**, 1131–1141. (doi:10.1016/j.compstruc.2010.11.004)
16. Lazarov BS, Schevenels M, Sigmund O. 2012 Topology optimization with geometric uncertainties by perturbation techniques. *Int. J. Numer. Methods Eng.* **90**, 1321–1336. (doi:10.1002/nme.3361)
17. Dunning PD, Kim HA, Mullineux G. 2011 Introducing loading uncertainty in topology optimization. *AIAA J.* **49**, 760–768. (doi:10.2514/1.J050670)
18. Da Silva G, Beck A, Cardoso E. 2018 Topology optimization of continuum structures with stress constraints and uncertainties in loading. *Int. J. Numer. Methods Eng.* **113**, 153–178. (doi:10.1002/nme.5607)
19. Kanno Y, Takewaki I. 2006 Robustness analysis of trusses with separable load and structural uncertainties. *Int. J. Solids Struct.* **43**, 2646–2669. (doi:10.1016/j.ijsolstr.2005.06.088)
20. Lógó J, Balogh B, Pintér E. 2018 Topology optimization considering multiple loading. *Comput. Struct.* **207**, 233–244. (doi:10.1016/j.compstruc.2017.03.018)
21. Luo Y, Zhou M, Wang MY, Deng Z. 2014 Reliability based topology optimization for continuum structures with local failure constraints. *Comput. Struct.* **143**, 73–84. (doi:10.1016/j.compstruc.2014.07.009)
22. Cuellar N, Pereira A, Menezes IF, Cunha A. 2018 Non-intrusive polynomial chaos expansion for topology optimization using polygonal meshes. *J. Braz. Soc. Mech. Sci. Eng.* **40**, 1–18. (doi:10.1007/s40430-018-1464-2)

23. Zhang XS, de Sturler E, Paulino GH. 2017 Stochastic sampling for deterministic structural topology optimization with many load cases: density-based and ground structure approaches. *Comput. Methods Appl. Mech. Eng.* **325**, 463–487. (doi:10.1016/j.cma.2017.06.035)
24. Young V, Querin OM, Steven G, Xie Y. 1999 3D and multiple load case bi-directional evolutionary structural optimization (BESO). *Struct. Optim.* **18**, 183–192. (doi:10.1007/BF01195993)
25. Xie Y, Steven GP. 1994 Optimal design of multiple load case structures using an evolutionary procedure. *Eng. Comput.* **11**, 295–302. (doi:10.1108/02644409410799290)
26. Csébfalvi A. 2018 Structural optimization under uncertainty in loading directions: benchmark results. *Adv. Eng. Softw.* **120**, 68–78.
27. Holmberg E, Thore C-J, Klarbring A. 2017 Game theory approach to robust topology optimization with uncertain loading. *Struct. Multidiscip. Optim.* **55**, 1383–1397. (doi:10.1007/s00158-016-1548-5)
28. Thore C-J, Alm Grundström H, Klarbring A. 2020 Game formulations for structural optimization under uncertainty. *Int. J. Numer. Methods Eng.* **121**, 165–185. (doi:10.1002/nme.6204)
29. Guest JK, Prévost JH, Belytschko T. 2004 Achieving minimum length scale in topology optimization using nodal design variables and projection functions. *Int. J. Numer. Methods Eng.* **61**, 238–254. (doi:10.1002/nme.1064)
30. Wang F, Lazarov BS, Sigmund O. 2011 On projection methods, convergence and robust formulations in topology optimization. *Struct. Multidiscip. Optim.* **43**, 767–784. (doi:10.1007/s00158-010-0602-y)
31. Bendsøe MP, Sigmund O. 1999 Material interpolation schemes in topology optimization. *Arch. Appl. Mech.* **69**, 635–654. (doi:10.1007/s004190050248)
32. Bendsøe MP. 1989 Optimal shape design as a material distribution problem. *Struct. Optim.* **1**, 193–202. (doi:10.1007/BF01650949)
33. Giraldo-Londoño O, Paulino GH. 2020 A unified approach for topology optimization with local stress constraints considering various failure criteria: von Mises, Drucker–Prager, Tresca, Mohr–Coulomb, Bresler–Pister and Willam–Warnke. *Proc. R. Soc. A* **476**, 20190861. (doi:10.1098/rspa.2019.0861)
34. Bertsekas DP. 1999 *Nonlinear programming*, 2nd edn. Nashua, NH: Athena Scientific.
35. Nocedal J, Wright S. 2006 *Numerical optimization*. Berlin/Heidelberg, Germany: Springer Science & Business Media.
36. Bourdin B. 2001 Filters in topology optimization. *Int. J. Numer. Methods Eng.* **50**, 2143–2158. (doi:10.1002/nme.116)
37. Zegard T, Paulino GH. 2016 Bridging topology optimization and additive manufacturing. *Struct. Multidiscip. Optim.* **53**, 175–192. (doi:10.1007/s00158-015-1274-4)
38. Zhou M, Lazarov BS, Sigmund O. 2014 Topology optimization for optical projection lithography with manufacturing uncertainties. *Appl. Opt.* **53**, 2720–2729. (doi:10.1364/AO.53.002720)
39. Lazarov BS, Wang F, Sigmund O. 2016 Length scale and manufacturability in density-based topology optimization. *Arch. Appl. Mech.* **86**, 189–218. (doi:10.1007/s00419-015-1106-4)
40. Clausen A, Andreassen E. 2017 On filter boundary conditions in topology optimization. *Struct. Multidiscip. Optim.* **56**, 1147–1155. (doi:10.1007/s00158-017-1709-1)
41. Wallin M, Ivarsson N, Amir O, Tortorelli D. 2020 Consistent boundary conditions for PDE filter regularization in topology optimization. *Struct. Multidiscip. Optim.* **62**, 1299–1311. (doi:10.1007/s00158-020-02556-w)
42. Spivak M. 1965 *Calculus on manifolds. A modern approach to classical theorems of advanced calculus*, p. 382 383. New York, NY: W. A. Benjamin, Inc.
43. Euler L. 1810 *Elements of algebra*, 2nd edn, p. 388 397. London, UK: J. Johnson and Company.
44. Faucette WM. 1996 A geometric interpretation of the solution of the general quartic polynomial. *Am. Math. Mon.* **103**, 51–57. (doi:10.1080/00029890.1996.12004698)
45. Senhora FV, Menezes IFM, Paulino GH. 2023 Topology optimization with local stress constraints and continuously varying load direction and magnitude: towards practical applications. Figshare. (doi:10.6084/m9.figshare.c.6423599)